

Ocean forcing of penultimate deglacial and last interglacial sea-level rise

Peter U. Clark^{1,9,*,#}, Feng He^{2,*}, Nicholas R. Golledge^{3,4}, Jerry X. Mitrovica⁵, Andrea Dutton⁶,
Jeremy S. Hoffman⁷, Sarah Dendy⁸

¹College of Earth, Ocean, and Atmospheric Sciences, Oregon State University, Corvallis, OR 97331, USA. ²Center for Climatic Research, Nelson Institute for Environmental Studies, University of Wisconsin–Madison, Madison, WI 53706, USA. ³Antarctic Research Centre, Victoria University of Wellington, Wellington 6140, New Zealand. ⁴GNS Science, Avalon, Lower Hutt 5011, New Zealand. ⁵Department of Earth and Planetary Sciences, Harvard University, Cambridge, MA, 02138. ⁶Department of Geological Sciences, University of Florida, Gainesville, FL 32611, USA. ⁷Science Museum of Virginia, 2500 West Broad Street, Richmond, VA 23220-2057, USA. ⁸Department of Geology, University of Illinois, Urbana-Champaign, IL 61801, USA. ⁹School of Geography and Environmental Sciences, University of Ulster, Coleraine, Northern Ireland BT52 1SA, UK. *These authors contributed equally to this work. #email: clarkp@onid.orst.edu

17 Sea-level histories during the two most recent deglacial-interglacial intervals experienced
18 significant differences¹⁻³ despite both periods having similar changes in global mean
19 temperature^{4,5} and forcing from greenhouse gases⁶. Although the last interglaciation (LIG)
20 experienced stronger boreal summer insolation forcing than during the present
21 interglaciation⁷, understanding why LIG global mean sea level may have been 6-9 m higher
22 than present has proven particularly challenging². During glacial as well as interglacial
23 periods, extensive areas of polar ice sheets were grounded below sea level, with grounding
24 lines and fringing ice shelves extending onto continental shelves⁸, suggesting that oceanic
25 forcing by subsurface warming may also have contributed to ice-sheet loss⁹⁻¹² analogous to
26 ongoing changes by the Antarctic^{13,14} and Greenland¹⁵ ice sheets. Such forcing would have
27 been especially effective during glacial periods when the Atlantic Meridional Overturning
28 Circulation (AMOC) experienced large variations on millennial timescales¹⁶, with a
29 reduction of the AMOC causing subsurface warming throughout much of the Atlantic
30 basin^{9,12,17}. Here we show that greater subsurface warming induced by the longer duration
31 of reduced AMOC during the penultimate deglaciation can explain the more-rapid sea-level
32 rise than during the last deglaciation. This greater forcing also contributed to excess loss
33 from the Greenland and Antarctic ice sheets during the LIG, causing global mean sea level
34 to rise at least 4 m above modern. When accounting for the combined influences of
35 penultimate and last-interglacial deglaciation on glacial isostatic adjustment, this excess loss
36 of polar ice during the LIG can explain much of the relative sea level recorded by fossil coral
37 reefs and speleothems at intermediate- and far-field sites.

38

39 Climate evolution over the last two terminations shares a number of similarities (Extended
40 Data Fig. 1). Proxy records of ocean circulation show that the last two terminations were
41 accompanied by large reductions of the AMOC. Climate responses to these reductions show the
42 characteristic bi-polar seesaw due to reduced northerly ocean heat transport and the weakening of
43 the Asian monsoon due to the cooling of the Northern Hemisphere. Other similarities include an
44 increase in the rate of sea-level rise when the AMOC begins to decrease and the occurrence of a
45 Heinrich event during the period of reduced AMOC. Similar climate changes accompanied earlier
46 terminations over the last 640 ka¹⁸, suggesting that an AMOC reduction is a characteristic feature
47 of these periods of rapid deglaciation.

48 There are also several notable differences between the last two terminations (Extended
49 Data Figs. 1, 2). First, proxy data suggest that the AMOC during T-II remained in a reduced state
50 for ~7,000 years before recovering at the start of the LIG. In contrast, during T-I, the AMOC only
51 remained weak for ~3,500 years before recovering to nearly full strength during the 1,500-year
52 Bølling-Allerød warm interval. It then decreased again during the 1,200-year Younger Dryas cold
53 interval, with its final recovery at the start of the present interglaciation. Second, the full T-II sea-
54 level rise occurred during the 7-kyr sustained “one-step” period of reduced AMOC, whereas only
55 ~50% of the T-I sea-level rise occurred during the ~6.5-kyr “two-step” period of reduced AMOC³
56 (Fig. 1). Third, ice-rafted debris (IRD) suggests that Heinrich event 11 (H11), which is nearly
57 twice as long as Heinrich event 1 (H1), was sourced from more than just the Hudson Strait Ice
58 Stream (HSIS), which was the primary source for H1¹⁹.

59 A transient simulation of T-I climate used an atmosphere-ocean general circulation model
60 (the National Center for Atmospheric Research Community Climate System Model version 3;
61 NCAR CCSM3) forced by changes in insolation, CO₂, ice sheets, and freshwater fluxes that, while

62 not in full agreement with reconstructions, were designed to cause the two-step reduction of the
63 AMOC¹⁷ (Fig. 1k). The simulation successfully captured many aspects of the climate evolution
64 through T-I as recorded by proxy records^{17,20,21}. Among the responses to the AMOC reduction was
65 subsurface warming throughout much of the Atlantic basin¹⁷ (Fig. 1k, 1l), which is supported by
66 proxy temperature records from intermediate-depth (1,000-1,500 m) North Atlantic core sites¹².

67 We used the same climate model to conduct a transient simulation that spans T-II and the LIG
68 (140-115 ka) (Methods). We applied freshwater forcing consistent with reconstructions that
69 reproduced the 7-kyr “one-step” reduction in the AMOC suggested by proxy records of ocean
70 circulation (Extended Data Figs. 1,3) in order to quantify associated changes in subsurface
71 temperatures during T-II and into the LIG and thus allow direct comparison with subsurface
72 warming simulated for T-I.

73 Fig. 1 compares forcing of ice-sheet surface mass balance from insolation, greenhouse
74 gases (GHGs), and low-latitude Pacific sea-surface temperatures (SSTs) for T-II and T-I to
75 representative examples of the simulated oceanic forcing at sites in the North (30°W, 45°N) (Fig.
76 1e, 1k) and South Atlantic (45°W, 70°S) (Fig. 1f, 1l). Changes in GHGs and SSTs are similar
77 during the two terminations, with increases of $\sim 2 \text{ W m}^{-2}$ from GHGs and $\sim 2^\circ\text{C}$ warming from low-
78 latitude Pacific SSTs, which strongly influence Northern Hemisphere ice-sheet surface mass
79 balance¹⁰. Despite these similarities, sea level reached modern by the end of T-II while it remained
80 $\sim 50\%$ below modern at the end of T-I (Fig. 1a, 1g). Some have attributed the faster rate of sea-
81 level rise during T-II to the greater boreal summer insolation forcing³, but that forcing only exceeds
82 that of T-I after the majority ($\sim 80 \text{ m}$) of T-II sea-level rise had occurred (Fig. 1a, 1b, Extended
83 Data Fig. 2). Otherwise, insolation forcing during the first 8,000 years of each termination is

84 similar ($\sim 55 \text{ W m}^{-2}$), whereas the associated 80 m of sea-level rise during T-II is much greater than
85 the $\sim 35 \text{ m}$ during T-I.

86 We attribute this contrast in sea-level response to the similar radiative forcing and
87 temperature changes of the last two terminations to the greater subsurface warming during T-II
88 associated with the “one-step” reduction in the AMOC than during the T-I “two-step” reduction,
89 leading to greater oceanic forcing of marine ice-sheet margins in the North (Fig. 1e, 1k, Extended
90 Data Fig. 4) and South (Fig. 1f, 1l, Extended Data Fig. 4) Atlantic. Moreover, the Eurasian Ice
91 Sheet during the Penultimate Glacial Maximum (PGM, $\sim 140 \text{ ka}$) was larger than during the Last
92 Glacial Maximum (LGM, $\sim 21 \text{ ka}$), with most of the excess mass located in low-lying areas south-
93 southeast of the glaciated Barents and Kara Seas²² that, from isostatic depression, was also marine
94 based (Extended Data Fig. 5). We thus hypothesize that collapse of this large marine-based ice
95 complex triggered by oceanic forcing would have also contributed to the rapid T-II sea-level rise,
96 with the associated IRD contribution to H11 diluting the contribution from the HSI¹⁹. In general,
97 this greater FW flux from deglaciating Northern Hemisphere ice sheets during T-II provided an
98 important positive feedback on that deglaciation through its influence on the AMOC and
99 subsurface temperatures.

100 Fig. 2 compares forcings during the last two interglaciations. Peak global mean SSTs were
101 similar (Fig. 2d, 2i) while LIG radiative forcing from CO_2 was only slightly higher ($\sim 0.25 \text{ W m}^{-2}$)
102 than during the present interglaciation (Fig. 2c, 2j). The main difference is in the higher boreal and
103 lower austral summer insolation forcing during the LIG (Fig. 2b, 2h). Modeling studies show that
104 this forcing would cause excess mass loss from the Greenland Ice Sheet during the LIG, but the
105 estimated 1-3 m of global mean sea-level equivalent (GMSLE) is too small to explain the LIG
106 highstand, thus requiring a contribution from the Antarctic Ice Sheet². Lower austral summer

107 insolation forcing during the LIG (Fig. 2b), however, results in surface cooling over most of
108 Antarctica, suggesting an important role for oceanic forcing, with warming hypothesized to
109 originate from an AMOC reduction during the LIG¹¹ or from a lagged ice-sheet response to
110 warming from a change in the strength and/or position of the Southern Ocean westerlies associated
111 with the T-II AMOC reduction³. One ice-sheet model simulates up to 6.7 m of sea-level rise when
112 specifying a uniform increase of Southern Ocean temperatures by 3°C¹¹.

113 Our transient climate simulation shows that T-II oceanic forcing in the Southern Ocean as
114 well as the North Atlantic continued into the early LIG (Fig. 2e, 2f, Extended Data Fig. 4). We use
115 the Parallel Ice Sheet Model (PISM) to assess the response of the Antarctic and Greenland ice
116 sheets to this oceanic as well as surface forcing through T-II and into the LIG as simulated by our
117 transient climate run (Methods). The Greenland Ice Sheet starts to deglaciate from its PGM extent
118 when adjacent ocean temperatures begin to warm at ~137.5 ka (Fig. 1e, Fig. 3g). It reaches its
119 present extent at 131.5 ka and then loses an additional 0.88 m GMSLE by 119.5 ka largely by
120 oceanic forcing of those sectors of the ice sheet that remain marine based, causing drawdown of
121 the ice-sheet interior (Fig. 3c). The majority (3.42 m) of the total sea-level rise (3.88 m) occurs
122 between 136-129 ka (Fig. 3g), corresponding to the period of rapid rise in global mean sea level
123 (GMSL) (Fig. 1a). Sensitivity tests in which ocean temperatures are held constant at either PGM
124 or LIG values show that the simulated deglaciation is controlled entirely by oceanic forcing
125 (Methods, Extended Data Fig. 6), supporting our hypothesis that oceanic forcing contributed to
126 deglaciation of other Northern Hemisphere ice sheets (Extended Data Fig. 4).

127 Our simulations also show that the major deglacial phase of the Antarctic Ice Sheet from
128 its PGM extent closely coincides with the onset of warming of adjacent ocean temperatures at
129 ~137.5 ka induced by the AMOC slowdown (Fig. 1f, Fig. 3g). In particular, the ice sheet retreats

130 to its present extent at ~128 ka, with the majority (6.25 m) of the total (6.65 m) sea-level rise also
131 occurring during the rapid T-II rise in global sea level (Fig. 3g). Sea-level rise then slows beginning
132 at 128 ka, followed by an acceleration starting at 126.5 ka, with a total of 2.99 m of LIG sea-level
133 rise occurring by 116 ka (Fig. 3g). The majority of this LIG deglaciation is associated with collapse
134 of the Amundsen Sea sector of the West Antarctic Ice Sheet (WAIS) (Fig. 3e) largely in response
135 to oceanic forcing (Extended Data Fig. 6), similar to what is suggested by observed recent changes
136 and projected for future ice-sheet recession in this area^{13,14}. This destabilization leads to retreat
137 that continues after the period of peak oceanic forcing at a rate that is determined largely by the
138 retrograde gradient of the bed beneath WAIS, followed by a slowing of retreat as the Southern
139 Ocean cools (Fig. 2f).

140 We next apply an ice-age sea-level model²³ to predict how our simulated changes in LIG
141 ice-sheet mass would be recorded at three widely distributed sites with well-dated corals that
142 provide minimum estimates of relative sea level (RSL) during the LIG^{24,25}, and a speleothem
143 record that bounds RSL during the same period²⁶ (Methods). Of the five adopted ice histories, the
144 two (LAM and HYB) based on studies that use a significantly larger Eurasian Ice Sheet during the
145 PGM relative to the LGM^{22,27} best predict RSL histories during the LIG that are consistent with
146 the elevation of the corals from the Bahamas, Western Australia and the Seychelles (Fig. 4a-c,
147 Extended Data Fig. 7). However, all simulations tend to underestimate the first half (prior to 122
148 ka) of the LIG RSL inferred from the speleothem record in Mallorca (Fig. 4d, Extended Data Fig.
149 7).

150 In the absence of melting of polar ice during the LIG, predictions of RSL at the Bahamas
151 and at Mallorca would show a monotonic rise, while those at the Seychelles and Western Australia
152 would tend to show a monotonic fall²⁸. Our ice-sheet simulations, however, are characterized by

153 excess melt from WAIS (relative to present day) that increases from 0 to 3 m GMSLE between
154 127 ka and 124 ka (Fig. 3g). This signal is responsible for the accentuated RSL rise over the same
155 period in the prediction for Bahamas and Mallorca and the reversal in the RSL trend at Western
156 Australia and the Seychelles (Fig. 4).

157 Our results do not account for several other processes that may have caused LIG global
158 mean and relative sea level to have been even higher than modeled here. For example, our
159 atmospheric modeling may underestimate surface melting around the lower-elevation margins of
160 the Greenland Ice Sheet. The greater boreal summer insolation forcing during the LIG relative to
161 the present interglaciation likely caused an even greater loss of glaciers, which today account for
162 0.41 m GMSLE. Warmer-than-present LIG temperatures would have caused additional
163 thermosteric sea-level rise⁵. Finally, we note that any additional melt near the start of the LIG
164 would change the preferred Earth models identified in our analysis (Methods). LIG RSL can also
165 be influenced by dynamic topography due to mantle convection, introducing meter-scale
166 displacement on these 10^5 -year timescales²⁹.

167 In summary, several lines of evidence suggest that the greater oceanic forcing during T-II
168 than during T-I, as simulated by our climate modeling, contributed to the more-rapid sea-level rise
169 during T-II. First, forcing of ice-sheet surface mass balance was similar during the two
170 terminations, indicating that an additional forcing was required to explain the differences in rates
171 of sea-level rise. Second, our GIA modeling demonstrates that the larger PGM Eurasian ice sheet
172 caused a significantly larger fraction of the ice-sheet bed to be below sea level, and thus be more
173 vulnerable to oceanic forcing, than during T-I. Third, our ice-sheet modeling shows that >85% of
174 the volume loss of the PGM Greenland and Antarctic ice sheets to their present sizes occurs in
175 response to oceanic forcing during T-II. Although additional modeling of the deglaciation of the

176 former NH ice sheets during T-II will be required to further support this hypothesis, our ice-sheet
 177 modeling does show that oceanic forcing was the primary driver of excess ice loss from the
 178 Greenland and Antarctic ice sheets during the LIG. Our sea-level predictions demonstrate that the
 179 modeled 4 m of GMSLE from LIG deglaciation of Greenland and Antarctic ice sheets may explain
 180 much of the LIG RSL at intermediate- and far-field sites when GIA from T-II deglaciation is
 181 included, although additional melt is required to fully reconcile these data.

182

- 183 1 Waelbroeck, C. *et al.* Sea-level and deep water temperature changes derived from benthic
 184 foraminifera isotopic records. *Quaternary Science Reviews* **21**, 295-305 (2002).
- 185 2 Dutton, A. *et al.* Sea-level rise due to polar ice-sheet mass loss during past warm periods.
 186 *Science* **349**, doi:10.1126/science.aaa4019 (2015).
- 187 3 Marino, G. *et al.* Bipolar seesaw control on last interglacial sea level. *Nature* **522**, 197-
 188 201, doi:10.1038/nature14499 (2015).
- 189 4 Marcott, S. A., Shakun, J. D., Clark, P. U. & Mix, A. C. A reconstruction of regional and
 190 global temperature for the past 11,300 years. *Science* **339**, 1198-1201 (2013).
- 191 5 Hoffman, J. S., Clark, P. U., Parnell, A. C. & He, F. Regional and global sea-surface
 192 temperatures during the last interglaciation. *Science* **355**, 276-279,
 193 doi:10.1126/science.aai8464 (2017).
- 194 6 Kohler, P., Nehrbass-Ahles, C., Schmitt, J., Stocker, T. F. & Fischer, H. A 156 kyr
 195 smoothed history of the atmospheric greenhouse gases CO₂, CH₄, and N₂O and their
 196 radiative forcing. *Earth System Science Data* **9**, doi:10.5194/essd-9-363-2017 (2017).
- 197 7 Berger, A. & Loutre, M.-F. Insolation values for the climate of the last 10 million years.
 198 *Quaternary Science Reviews* **10**, 297-317 (1991).
- 199 8 Hughes, T., Denton, G. H. & Grosswald, M. G. Was There a Late-Wurm Arctic Ice
 200 Sheet. *Nature* **266**, 596-602, doi:DOI 10.1038/266596a0 (1977).
- 201 9 Shaffer, G., Olsen, S. M. & Bjerrum, C. J. Ocean subsurface warming as a mechanism for
 202 coupling Dansgaard-Oeschger climate cycles and ice-rafting events. *Geophysical*
 203 *Research Letters* **31**, L24202, doi:24210.21029/22004GL020968 (2004).
- 204 10 Clark, P. U., Hostetler, S. W., Pisias, N. G., Schmittner, A. & Meisner, K. J. in *Ocean*
 205 *Circulation: Mechanisms and Impacts* Vol. 173 (eds A. Schmittner, J. Chiang, & S.
 206 Hemming) 209-246 (American Geophysical Union, Geophysical Monograph, 2007).
- 207 11 DeConto, R. M. & Pollard, D. Contribution of Antarctica to past and future sea-level rise.
 208 *Nature* **531**, 591-597, doi:10.1038/nature17145 (2016).
- 209 12 Marcott, S. A. *et al.* Ice-shelf collapse from subsurface warming as a trigger for Heinrich
 210 events. *Proceedings of the National Academy of Sciences of the United States of America*
 211 **108**, 13415-13419 (2011).
- 212 13 Joughin, I., Smith, B. E. & Medley, B. Marine ice sheet collapse potentially under way
 213 for the Thwaites Glacier basin, West Antarctica. *Science* **344**, 735-738 (2014).

- 214 14 Rignot, E., Mouginot, J., Morlighem, M., Seroussi, H. & Scheuchl, B. Widespread, rapid
215 grounding line retreat of Pine Island, Thwaites, Smith, and Kohler glaciers, West
216 Antarctica, from 1992 to 2011. *Geophysical Research Letters* **41**, 3502-3509 (2014).
- 217 15 Wood, M. *et al.* Ocean-induced melt triggers glacier retreat in northwest Greenland.
218 *Geophysical Research Letters* **45**, 8334-8342, doi:10.1029/2018gl078024 (2018).
- 219 16 Bohm, E. *et al.* Strong and deep Atlantic meridional overturning circulation during the
220 last glacial cycle. *Nature* **517**, 73-76, doi:10.1038/nature14059 (2015).
- 221 17 Liu, Z. *et al.* Transient simulation of last deglaciation with a new mechanism for Bolling-
222 Allerod warming. *Science* **325**, 310-314 (2009).
- 223 18 Cheng, H. *et al.* The Asian monsoon over the past 640,000 years and ice age
224 terminations. *Nature* **534**, 640-646, doi:10.1038/nature18591 (2016).
- 225 19 Obrochta, S. P. *et al.* Climate variability and ice-sheet dynamics during the last three
226 glaciations. *Earth and Planetary Science Letters* **406**, 198-212,
227 doi:10.1016/j.epsl.2014.09.004 (2014).
- 228 20 Shakun, J. D. *et al.* Global warming preceded by increasing carbon dioxide
229 concentrations during the last deglaciation. *Nature* **484**, 49-55 (2012).
- 230 21 He, F. *et al.* Northern Hemisphere forcing of Southern Hemisphere climate during the last
231 deglaciation. *Nature* **494**, 81-85 (2013).
- 232 22 Lambeck, K. *et al.* Constraints on the Late Saalian to early Middle Weichselian ice sheet
233 of Eurasia from field data and rebound modelling. *Boreas* **35**, 539-575, doi:Doi
234 10.1080/03009480600781875 (2006).
- 235 23 Kendall, R. A., Mitrovica, J. X. & Milne, G. A. On post-glacial sea level - II. Numerical
236 formulation and comparative results on spherically symmetric models. *Geophysical*
237 *Journal International* **161**, 679-706 (2005).
- 238 24 Dutton, A. & Lambeck, K. Ice volume and sea level during the Last Interglacial. *Science*
239 **337**, 216-219, doi:10.1126/science.1205749 (2012).
- 240 25 Dutton, A., Webster, J. M., Zwartz, D., Lambeck, K. & Wohlfarth, B. Tropical tales of
241 polar ice: evidence of Last Interglacial polar ice sheet retreat recorded by fossil reefs of
242 the granitic Seychelles islands. *Quaternary Science Reviews* **107**, 182-196,
243 doi:10.1016/j.quascirev.2014.10.025 (2015).
- 244 26 Polyak, V. J. *et al.* A highly resolved record of relative sea level in the western
245 Mediterranean Sea during the last interglacial period. *Nature Geoscience* **11**, 860-864,
246 doi:10.1038/s41561-018-0222-5 (2018).
- 247 27 Colleoni, F., Wekerle, C., Naslund, J. O., Brandefelt, J. & Masina, S. Constraint on the
248 penultimate glacial maximum Northern Hemisphere ice topography (approximate to 140
249 kyrs BP). *Quaternary Science Reviews* **137**, 97-112, doi:10.1016/j.quascirev.2016.01.024
250 (2016).
- 251 28 Dendy, S., Austermann, J., Creveling, J. R. & Mitrovica, J. X. Sensitivity of Last
252 Interglacial sea-level high stands to ice sheet configuration during Marine Isotope Stage
253 6. *Quaternary Science Reviews* **171**, 234-244, doi:10.1016/j.quascirev.2017.06.013
254 (2017).
- 255 29 Austermann, J., Mitrovica, J. X., Huybers, P. & Rovere, A. Detection of a dynamic
256 topography signal in last interglacial sea-level records. *Science Advances* **3**,
257 doi:10.1126/sciadv.1700457 (2017).
- 258

259 **Acknowledgments** This work was funded by the US National Science Foundation (NSF) through
260 grants AGS-1503032 (to P.U.C.), AGS-1502990 (to F.H.) OCE-1702684 (to J.X.M.), and
261 1559040 (to A.D.); the NOAA Climate and Global Change Postdoctoral Fellowship program,
262 administered by the University Corporation for Atmospheric Research (to F.H.); contract
263 VUW1501 from the Royal Society Te Aparangi with support from the Antarctic Research Centre,
264 Victoria University of Wellington (to N.R.G.); contract CO5X1001 to GNS Science from the
265 Ministry for Business, Innovation and Employment (to N.R.G.); and Harvard University (J.X.M.).
266 We acknowledge high-performance computing support from Yellowstone (ark:/85065/d7wd3xhc)
267 provided by NCAR's Computational and Information Systems Laboratory, sponsored by the NSF.
268 This research used resources of the Oak Ridge Leadership Computing Facility at the Oak Ridge
269 National Laboratory, which is supported by the Office of Science of the US Department of Energy
270 under Contract No. DE-AC05-00OR22725. PISM is supported by NASA grants NNX13AM16G
271 and NNX13AK27G. We thank Jason Box, Christo Buizert, and Anais Orsi for discussions.
272

273 **Author contributions** F.H. performed the GCM modeling; N.R.G. performed the ice-sheet
274 modeling; J.X.M. performed the sea-level modeling with help from S.D.; P.U.C., A.D. and J.S.H.
275 performed the data analysis; P.U.C., F.H., N.R.G., and J.X.M. wrote the manuscript; all authors
276 discussed the results and contributed towards improving the final manuscript.
277

278 **Competing interests** The authors declare no competing interests.
279

280 **Reprints and permissions information** is available at <http://www.nature.com/reprints>.
281

282 **Correspondence and requests for materials** should be addressed to P.U.C.
283
284
285

286 **Fig. 1. Sea-level change and climate forcings during the penultimate and last deglaciations.**

287 **a, g**, Records of relative and global mean sea level (Methods, Extended Data Fig. 2). Uncertainty
288 on blue line is 1σ ; uncertainty on coral data (circles) is 2σ . **b, h**, June 21 insolation for 65°N ⁷. **c, i**,
289 Radiative forcing from greenhouse gases (CO_2 , CH_4 , and N_2O)⁶. Uncertainty is square root of the
290 sum of squares of the uncertainties of the individual greenhouse gases. **d, j**, Tropical (23.5°N-S)
291 mean annual sea-surface temperature stack with 2 s.d. relative to the HadISST1.1 1870–1889
292 data^{4,5}. **e, k**, Changes in the model maximum Atlantic meridional overturning transport (below 500
293 m) (black line) and of temperature as a function of time and depth at 30°W , 45°N relative to 140
294 ka (**e**) and 22 ka¹⁷ (**k**) as simulated by the NCAR CCSM3 (Methods). **f, l**, Evolution of temperature
295 as a function of time and depth at 45°W , 70°S relative to 140 ka (**f**) and 22 ka¹⁷ (**l**) as simulated by
296 the NCAR CCSM3 (Methods).

297

298 **Fig. 2. Sea level and climate forcings during the last and present interglaciations. a, g**, Records

299 of relative and global mean sea level (Methods, Extended Data Fig. 2). Uncertainty on coral data
300 (circles) is 2σ . **b, h**, June 21 insolation for 65°N ⁷. **c, i**, Radiative forcing from greenhouse gases
301 (CO_2 , CH_4 , and N_2O)⁶. Uncertainty is the square root of the sum of squares of the uncertainties of
302 the individual greenhouse gases. **d, j**, Global mean annual sea-surface temperature stack with 2
303 s.d. relative to the HadISST1.1 1870–1889 data^{4,5}. **e, k**, Evolution of temperature as a function of
304 time and depth at 30°W , 45°N relative to 140 ka (**e**) and 22 ka¹⁷ (**k**) as simulated by the NCAR
305 CCSM3 (Methods). **f, l**, Evolution of temperature relative to 140 ka as a function of time and depth
306 at 45°W , 70°S relative to 140 ka (**f**) and 22 ka¹⁷ (**l**) as simulated by the NCAR CCSM3 (Methods).

307

308 **Fig. 3. Simulations of the Greenland and Antarctic ice sheets. a,** The Greenland Ice Sheet at
 309 the Penultimate Glacial Maximum. Logarithmic scale bar for velocity fields shown by color
 310 scheme; contours on ice sheet are for surface elevation in meters. **b,** The Greenland Ice Sheet at
 311 116 ka. Logarithmic scale bar for velocity fields shown by color scheme; contours on ice sheet are
 312 for surface elevation in meters. **c,** Difference in thickness of the Greenland Ice Sheet between 116
 313 ka and present day. Contours on ice surface and color scheme show change in thickness. **d,** The
 314 Antarctic Ice Sheet at the Penultimate Glacial Maximum. Logarithmic scale bar for velocity fields
 315 shown by color scheme; contours on ice sheet are for surface elevation in meters. **e,** The Antarctic
 316 Ice Sheet at 116 ka. Logarithmic scale bar for velocity fields shown by color scheme; contours on
 317 ice sheet are for surface elevation in meters. **f,** Change in thickness of the Antarctic Ice Sheet
 318 between 116 ka and present day. Contours on ice surface and color scheme show change in
 319 thickness. **g,** Contributions of the Greenland and Antarctic Ice Sheets to global mean sea level
 320 between 140 ka and 116 ka.

321

322 **Fig. 4. Predictions of relative sea level at four far-field sites. a,** Relative sea-level (RSL) data
 323 from the Bahamas based on well-dated corals compared to a prediction of RSL using our simulated
 324 LIG loss from the Greenland and Antarctic Ice Sheets and the LAM ice history²² (solid green line)
 325 and the HYB ice history (solid blue line) (see Methods). Also shown are predictions of RSL using
 326 just the LAM ice history²² (dashed green line) and the HYB ice history (dashed blue line). **b, c,** As
 327 in **a**, except for Western Australia (**b**) and the Seychelles (**c**). Uncertainties are for age (2σ),
 328 elevation (downward) and coral-depth habitat (upward). **d,** RSL data from Mallorca based on
 329 speleothem records. Uncertainties are for age (2σ) and growth. The Earth models used in the
 330 calculations are characterized by a lithospheric thickness, and upper and lower mantle viscosity

331 of: 140 km, 0.3×10^{21} Pas, 8.0×10^{22} Pa s (**a**), 96 km, 0.3×10^{21} Pas, 5.0×10^{22} Pa s (**b**), 30 km,
332 0.5×10^{21} Pas, 3.0×10^{22} Pa s (**c**), and 120 km, 2.0×10^{21} Pas, 8.0×10^{22} Pa s (**d**). Each of the
333 coral records are comprised of data collected from multiple sites and the RSL predictions are
334 shown for the following representative locations: 24.05°N , 285.47°E (**a**), 21.97°S , 113.93°E (**b**),
335 4.28°S , 55.73°E (**c**), and 39.61°N , 3.38°E (**d**). The consistency between the data and the
336 predictions would be unaffected if we plotted RSL histories at each location that accounted for the
337 variable collection sites.

338 **Methods**

339 **Transient climate modeling.** We use the fully-coupled configuration of the Community Climate
340 System Model version 3 (CCSM3) in T31 resolution³⁰ for the transient simulation of the
341 penultimate deglaciation and last interglaciation (LIG) from 140 to 120 ka. CCSM3 was used in
342 the TraCE-21K transient simulation of the past 21,000 years spanning the last deglaciation and the
343 current interglaciation^{17,21,31}. The transient simulation of the penultimate deglaciation was
344 initialized with a 600-year equilibrium simulation of the penultimate glacial maximum that
345 branched off the TraCE-21K last glacial maximum (LGM) simulation with orbital configuration⁷
346 and greenhouse gas contribution (CO₂) for 140 kyr³². The transient simulation of penultimate
347 deglaciation with CCSM3 was integrated from 140 ka to 129 ka with changing atmospheric
348 greenhouse gas concentrations³², Earth's orbit⁷, and continental ice sheets based on ICE-5G³³ but
349 with the timing of the corresponding sea-level rise adjusted to closely follow the Waelbroeck et
350 al.¹ and Grant et al.³⁴ sea-level reconstructions for the penultimate deglaciation (Extended Data
351 Figs. 2, 3). We note that our sea-level modeling suggests that the sizes of the penultimate glacial
352 maximum Northern Hemisphere ice sheets differed from the LGM and thus our climate modelling
353 does not account for these important differences between the two terminations. Further climate
354 modeling is thus needed to assess how these differences may have affected atmospheric circulation
355 over the North Atlantic Ocean and the AMOC.

356 To simulate the impact of freshwater forcing from Heinrich event 11 on the Atlantic
357 Meridional Overturning Circulation, freshwater is added at the surface of the North Atlantic in the
358 area between 50°-70°N, being ramped to 0.17 Sverdrups (Sv; 10⁶ m³ s⁻¹) from 138 ka to 135.5 ka
359 where it remains until 129.7 ka when it is shut off (Extended Data Fig. 3). The transient simulation
360 of the LIG with CCSM3 was integrated from 129 ka to 116 ka with changing orbits and

361 atmospheric greenhouse gases under present-day ice-sheet configuration. No additional freshwater
362 fluxes were applied during the transient simulation of the LIG.

363 **Ice-sheet modeling.** We use version 0.7.1 of the Parallel Ice Sheet Model (PISM), in which the
364 dynamical core superposes velocity fields from the shallow shelf and shallow ice approximations
365 across the entire domain. Fast flow (“streaming”) of grounded ice is enabled by plastic failure of
366 subglacial sediments, which depends on a prescribed but spatially-variable till friction angle,
367 representing sediment strength and its degree of saturation. The till friction angle is based primarily
368 on topography, so that deeper areas have lower friction angles. This mimics the effect of weaker
369 sediments accumulating in deeper basins. The parameterization follows the form, $\phi_{min} / \phi_{max} /$
370 $elevation_{min} / elevation_{max}$, in which the ϕ_{min} is the friction angle applied
371 below $elevation_{min}$, ϕ_{max} is the friction angle applied above $elevation_{max}$, and values in
372 between are linearly interpolated. For our Greenland simulations we prescribe values of 10 / 30 /
373 -300 / 300, and for Antarctica 6 / 30 / -700 / -100. These values are based on, but modified from,
374 previous work (Aschwanden et al.³⁵ for Greenland; Golledge et al.³⁶ for Antarctica), but these
375 values are uncertain. Our values were chosen following exploratory simulations that sought to best
376 capture the broad-scale geometric and dynamic features of the ice sheets.

377 Sediment strength evolves dynamically depending on the basal ice temperature. Where ice
378 is sufficiently thick to allow basal melting, meltwater weakens the substrate until driving stresses
379 exceed till cohesion. Failure of the substrate that results in acceleration of overlying ice follows a
380 pseudo-plastic law^{37,38}, such that a small increase in stress above the shear strength of the substrate
381 leads to an increasing velocity response. This ultimately thins the ice, which reduces the
382 gravitational driving stress and results in a deceleration of the ice sheet. The cyclic behavior of ice
383 streams that occurs as a consequence of this mechanism is described in more detail elsewhere³⁹.

384 PISM uses a sub-grid grounding line scheme⁴⁰ in which the interpolation of sub-ice shelf melt
385 across the grounded to floating transition may be turned on or off. When turned on, the scheme
386 tends to accelerate ice-sheet retreat in marine basins, whereas when it is off, the scheme produces
387 a slower response³⁶. This difference in behavior results in differences in retreat rates, but
388 equilibrium states (for example, ice volume) are less affected. In our experiments we investigated
389 both approaches, and found that interpolating sub-shelf melt across the grounding line produced
390 simulations that were most closely in keeping with geological constraints for Termination I (T-I)
391 (see below).

392 We also used a range of enhancement factors for the shallow ice (SIAe) and shallow shelf
393 (SSAe) equations (SIAe = 1, 2, 3; SSAe = 0.5, 1), and different values for the basal sliding
394 exponent that controls how plastic or linear the substrate deformation response to applied driving
395 stresses ($q = 0.25, 0.6$). Floating ice is controlled by two calving mechanisms – one based on
396 horizontal strain rates⁴¹ and another that prescribes a minimum thickness criterion (50 m for
397 Greenland, 200 m in Antarctica).

398 We run separate simulations for the Greenland and Antarctic ice sheets, both at 20-km
399 resolution. To drive our ice-sheet model, we use output climatologies from the transient CCSM3
400 simulations described above for T-I and Termination II (T-II). Atmospheric outputs are applied as
401 anomalies to present-day air temperature and precipitation fields^{42,43}, in the same manner as
402 employed previously⁴⁴. We employ a positive-degree day (PDD) model to translate temperatures
403 above freezing into surface melt, of which 60% remains in the snowpack as a consequence of
404 refreezing during percolation. The proportion of refreezing that takes place even under present
405 conditions is difficult to constrain precisely⁴⁵ so we use a uniform value both for the control and
406 perturbation experiments, in order to minimize the effects of this parameterization. That is,

407 differences in the simulation outputs are unlikely to arise from uncertainty in this aspect of model
408 parameterization.

409 During our model tuning process, we explored a wide range of degree-day values (from 1
410 mm °C⁻¹ day⁻¹ up to 64 mm °C⁻¹ day⁻¹) independently for both snow and ice. We tried the more
411 usual melt threshold of 273 K and the lower value of 270 K following van den Broeke et al.⁴⁶. The
412 latter method yields more widespread melt, mimicking the possible melt arising from short-wave
413 radiation under sub-freezing conditions, and thus degree-day factors are typically lower (van den
414 Broeke et al., 2010). We also allow for stochastic variability in daily temperatures using a zero-
415 mean white noise component whose standard deviation is set at 5 K. Although the choice of PDD
416 parameters did exert some control on the geometry of the evolving ice mass, the basic shape of the
417 ice sheet evolved in a similar manner regardless of either the melt forcing or the glaciological
418 parameterization, suggesting that the dominant control on ice-sheet geometry is the climate forcing
419 from the GCM. Recent work has shown that our simulations of surface mass balance (SMB) of
420 the Greenland Ice Sheet under the high boreal summer insolation of the LIG may be sensitive to
421 climate model resolution and SMB model type (i.e., PDD, surface energy balance)⁴⁷.

422 Oceanic fields for temperature and salinity at 500 m depth were used as inputs to a
423 thermodynamic ocean model that calculates basal melt from salt and heat-flux gradients across the
424 ice/ocean interface, according to the scheme described in⁴⁸. As with the atmospheric variables, we
425 apply the oceanic fields as anomalies from a present-day ocean configuration that for Antarctica
426 is tuned to reproduce observed melt-rate patterns⁴⁹. Since such constraints are not currently
427 available for Greenland, we use a spatially uniform melt factor instead, which is iteratively refined
428 so that both LGM and present-day ice-sheet extents are reproduced (see below). Ice thickness and
429 bed topography for the two ice sheets are taken from the most recent compilations^{50,51}.

430 With the model set-up as described above, we ran a series of time-evolving experiments
431 that first focused on T-I, rather than T-II. The rationale for this approach is that substantial
432 geological data exist with which to constrain the evolving ice-sheet geometry through the last
433 deglaciation, whereas there are few constraints for the preceding T-II. Therefore, in order to
434 optimize our parameter settings, we undertook >500 experiments of T-I for both ice sheets until a
435 good fit to empirical constraints was found. For Antarctica, our guiding constraints are that the ice
436 sheet at the LGM, immediately prior to T-I, should occupy the majority of the continental shelf,
437 and have an ice-volume excess above present that is within the range of 5.6-14.5 m represented by
438 previous simulations⁵²⁻⁵⁵. Furthermore, we required that the evolution of the simulated ice sheet
439 must reproduce the glacial maximum thickening of West Antarctica and thinning of East
440 Antarctica inferred from ice-core analyses⁵⁵, and exhibit a pattern of mass loss that is consistent
441 with geologically inferred deglacial changes in ice discharge⁵⁶. In Greenland, geological
442 constraints on the offshore extent of the LGM ice sheet are sparse, but the ice volume excess is
443 thought to have been in the range 2 – 5 m global mean sea level equivalent^{57,58}. We use this range
444 as our target (Extended Data Fig. 8). Finally, both ice sheets are required to reproduce present-day
445 grounded ice extent and volume as closely as possible at the end of the T-I simulations.

446 Once this phase of parameter optimization is complete, we run our experiments for T-II
447 using the exact same settings, changing only the input climatology based on outputs from CCSM3.
448 This dual approach allows for the robust simulation of a period, such as T-II, for which little data
449 exist to constrain outputs. In addition, this methodology allows for the direct comparison of model
450 outputs for the two periods, allowing any differences to be attributed solely to the imposed climate
451 forcing rather than to uncertainties in the modelling procedure. Finally, by tuning the model to fit
452 relatively well-known constraints such as LGM and present-day extent and volume, we reduce the

453 influence of any inaccuracies in the climate model representation of air or ocean temperatures
454 during the periods of simulation. Thus, if CCSM3 under- or overestimates the magnitude of past
455 climate anomalies with respect to present, the internal consistency between the T-I and T-II climate
456 simulations coupled with the data-constrained simulation of T-I mean that the reliability of the T-
457 II simulation is unaffected.

458 A novelty of our ice-sheet simulations compared to previous studies^{59,60} is that we use a
459 fully evolving T-I experiment to constrain our model parameterizations. This includes components
460 such as degree-day factors for the PDD scheme. For Greenland, we run an ensemble of tuning
461 experiments that explore a range of snow and ice melt factors as well as ice-flow enhancement
462 coefficients (Extended Data Fig. 8). By then selecting the parameterization that at the end of the
463 T-I simulation most closely reproduces present-day ice volume and geometry we ensure that the
464 surface melt fields we generate are realistic. We then apply this setup to our T-II experiments. Our
465 annual temperature range is defined by the CCSM3 outputs. However, we also experimented with
466 duplicate simulations in which we modified our Greenland climatologies to incorporate summer
467 temperatures from Fausto et al.⁴². These simulations resulted in only minor differences in mass
468 change, suggesting that in our experiments, atmospheric forcing plays a lesser role than oceanic
469 forcing (Extended Data Figs. 6, 9). This is supported by experiments in which we also explored
470 alternative grounding line schemes to make the ice sheets either more or less sensitive to ocean
471 temperature change. In the less sensitive experiments, the ice sheet failed to advance sufficiently
472 far offshore, and was thus incompatible with geological constraints.

473 **Predictions of relative sea level.** Calculations of glacial isostatic adjustment described in the text
474 are based on a pseudo-spectral sea-level theory²³ for the case of spherically symmetric (i.e.,
475 rheology varies with depth alone), Maxwell viscoelastic Earth models, with a truncation at

476 spherical harmonic degree and order 256. The theory incorporates time-varying coastlines,
477 changes in the perimeter of grounded, marine-based ice sheets, and the impact on sea level of load-
478 induced perturbations to the Earth's rotation axis, where these perturbations are computed using
479 the rotational stability theory of Mitrovica et al.⁶¹. Profiles of the density and elastic structure of
480 the Earth model are taken from the seismic Preliminary Reference Earth Model⁶². The viscosity
481 structure of the Earth models is defined by three layers, a lithospheric zone of infinite viscosity,
482 and sub-lithospheric upper and lower mantle regions, where the boundary between the latter two
483 regions is taken to be 670 km depth. The thickness of the lithosphere and the viscosity of the upper
484 and lower mantle are free parameters of the modeling and are varied, respectively, within the
485 following ranges: 30 – 140 km; 2-20 X 10²⁰ Pa s; and 2-100 X 10²¹ Pa s.

486 The set of five ice histories adopted in this study are based, in part, on histories constructed
487 by Dendy et al.²⁸ in their investigation of the sensitivity of LIG sea level predictions to variations
488 in the timing and geometry of ice cover during Marine Isotope Stage 6. We begin by summarizing
489 these ice histories.

490 All models in Dendy et al.²⁸ use the ICE6G ice history⁶³ for the period extending from the
491 LGM to present day and they extend back four full glacial cycles. The models are constrained to
492 have interglacial ice volumes and geometry identical to present-day ice cover on the Earth (i.e.,
493 there is no excess ice melting during previous interglaciations, including the LIG). The so-called
494 WAE ice model adopts the eustatic sea-level curve estimated by Waelbroeck et al.¹ on the basis of
495 benthic foraminifera isotope records. In the period prior to the LGM, the ice geometry is
496 constrained to be identical to the geometry post-LGM whenever the eustatic values are identical.
497 The LAM and COL models in Dendy et al.²⁸ also adopt the pre-LGM eustatic curve of Waelbroeck
498 et al.¹, but are distinguished from WAE by their ice history during the penultimate glacial cycle.

499 In particular, these models adopt the ice geometry during the penultimate glacial maximum (PGM)
500 inferred by Lambeck et al.²² and Colleoni et al.²⁷, which are both characterized by more significant
501 ice cover over Eurasia during the PGM than the LGM. Since the difference in peak Eurasian ice
502 volume during the PGM in the LAM and COL models is large (55 m and 71 m, respectively, in
503 units of equivalent GMSL), we have constructed an intermediate ice history (HYB) that is
504 essentially the average of these models (peak volume of 66 m GMSL equivalent during the PGM)
505 The increased ice cover of the LAM, HYB and COL models relative to the WAE model is
506 compensated, in large part, by a reduction of the volume of the Laurentide Ice Sheet during the
507 PGM relative to the LGM^{22,27}. All four models, WAE, LAM, HYB and COL, converge to the same
508 ice geometry (i.e., the present-day ice geometry) at the beginning of the model LIG. We note that
509 we have adapted the WAE, LAM and COL models described by Dendy et al.²⁸ to more closely
510 follow the eustatic curve of Waelbroeck et al.¹. Finally, the model SHA in Dendy et al.²⁸ is
511 constructed in a manner identical to WAE, with the exception that the model adopts the eustatic
512 curve derived by Shakun et al.⁶⁴ in the period prior to the LGM.

513 The ice histories considered in the present study combine the five models described above
514 with the Antarctic and Greenland Ice Sheet histories discussed in the main text. Specifically, the
515 difference in ice height during the period from 140 ka to 116 ka relative to the present day in the
516 ice-sheet simulations of the main text are applied to each of the Dendy et al.²⁸ models. The net
517 result is that the five models constructed in this manner are characterized, in contrast to those in
518 Dendy et al.²⁸, with excess melting of the Antarctic and Greenland Ice Sheets during the LIG
519 relative to present-day. We ran 337 Earth models for each of the five ice histories (total of 1685
520 simulations) in which parameters defining the Earth model were varied over plausible ranges.

521 In exploring the fit of the relative sea level (RSL) predictions to the coral record, we
522 considered three sites that have the largest data sets of well-dated corals (Bahamas, Seychelles and
523 Western Australia) and a relatively new speleothem data set from Mallorca (43) (Extended Data
524 Fig. 7). Given that corals provide a minimum bound on sea level, our metric for fit for these data
525 was the number of coral records that any specific RSL prediction bounded from above. In contrast,
526 we interpret the height uncertainties associated with the published speleothem data to represent a
527 two-way bound on peak RSL.

528 None of the 1685 simulations (i.e., our sampling of 337 Earth models and 5 ice histories)
529 were successful in bounding all coral records from above. As an indication of performance,
530 Extended Data Fig. 7 shows predictions from the full suite of simulations that satisfy the following
531 criteria: (1) all coral data from Western Australia and Bahamas, with the exception of the earliest
532 datum at the latter site (at ~131 ka), fall below the prediction; and (2) the prediction at the
533 Seychelles falls above all three coral records at an elevation of ~4 m. The various lines on the
534 figure represent the different Earth models for each ice history that satisfy these constraints. For
535 each ice history (i.e., each column of Extended Data Fig. 7), the Earth models sampled on each
536 frame (i.e., each site) represent a discrete set that may or may not overlap with the set from a
537 different site. As an example, in the case of the LAM and COL ice histories, no single Earth model
538 appears on the results for all three sites. This is reflected in Fig. 4 in the main text, where the
539 simulation highlighted in each frame is the result for a distinct Earth model. This variation is
540 justified by the fact that the Earth's mantle is subject to large amplitude variations in viscoelastic
541 structure and so it would be unexpected if the sea-level response at each of the three sites preferred
542 the same Earth model.

543 Note that the number of simulations that satisfy our plotting criterion for the Bahamas
544 increases as one moves to ice histories with larger Eurasian ice cover at the PGM (i.e., from the
545 WAE to the COL results), but the number of simulations that satisfy the criteria for the Seychelles
546 decreases in the same sense. While not apparent from Extended Data Fig. 7, the predicted
547 highstand at Seychelles increases as one considers Earth models with progressively thinner elastic
548 lithospheres (see Ref. 28, Fig. 9A), and the simulations that predict RSL highstands above the
549 Seychelles records are those based on a lithospheric thickness of 30 km (as in Fig. 4 of the main
550 text) or, in a couple of cases for the WAE ice history, 50 km. This raises two important issues.
551 First, none of the simulations that yield RSL above all the coral elevations at Seychelles also satisfy
552 the geological constraints at the Bahamas. Second, since the predicted highstand at the Seychelles
553 is sensitive to the adopted lithospheric thickness, there is a trade-off between the preferred value
554 of this parameter and the level of excess melting during the LIG. That is, increasing polar ice sheet
555 melting above the ~4 m GMSL equivalent adopted in the simulations in Extended Data Fig. 7,
556 would increase the range of lithospheric thickness that would satisfy the Seychelles coral record,
557 and thus bring the inference into better accord with other GIA-based estimates of this Earth model
558 parameter.

559 This issue may also have relevance in regard to the results for Mallorca (Extended Data
560 Fig. 7) where simulations are only plotted if the misfit between the GIA predictions and the
561 speleothem observations is within 50% of the minimum misfit achieved in all simulations. In this
562 case, fewer of the simulations provide a reasonable fit to the speleothem record as one considers
563 ice histories with progressively larger volumes over Eurasia at PGM and, indeed, no simulations
564 based on the COL ice history satisfy our plotting criterion. However, regardless of the adopted ice
565 history, none of the simulations fit the highstand constraints before 125 ka. Bringing the GIA

566 predictions in Extended Data Fig. 7 into accord with the Mallorca observations would require
567 additional excess melting that is limited to the earliest phase of the LIG.

568 As a final point, simulations based on the SHA ice history yielded misfits significantly
569 larger than predictions shown in Extended Data Fig. 7.

570 The sea-level simulations described above yield changes in sea level and topography at
571 each time slice of the ice history. As an example, Extended Data Fig. 5 shows the reconstructed
572 topography for the area covered by the Scandinavian Ice Sheet at 131 ka, near the end of the MIS6
573 deglaciation, for a simulation based on the LAM ice history and a specific Earth model (see
574 caption). The map supports the suggestion in the main text that the margin of grounded ice
575 complexes in this region across MIS 6 through 5e were marine based.

576 **Evidence for warming over the Greenland Ice Sheet during the Last Interglaciation.** Here we
577 evaluate the evidence for warming over the Greenland Ice Sheet during the Last Interglaciation
578 (LIG). This supports our climate model simulation that while the LIG atmosphere was warmer
579 than pre-Industrial, it largely remained below freezing and did not lead to significant mass loss
580 from surface melting.

581 Regarding the reconstructed LIG temperatures at the NEEM⁶⁵ and GISP2⁶⁶ ice-core sites,
582 there is uncertainty in which $d\delta^{18}\text{O}_{\text{ice}}/dT$ relationship should be used to reconstruct LIG
583 temperatures, and this uncertainty is exacerbated when applying the modern $d\delta^{18}\text{O}_{\text{ice}}-dT$
584 relationship to past climates, where differences in orbital forcing, moisture transport pathways,
585 ice-sheet topography, and sea-ice extent can change the relationship⁶⁷⁻⁷². To illustrate some of
586 these uncertainties, we have compared our simulated temperatures for the NEEM and GISP2 ice-
587 core sites with the temperature reconstructions for these sites based on $\delta^{18}\text{O}_{\text{ice}}$ (Extended Data Fig.
588 10). These reconstructions span the interval 127-120 ka, which is the warmest interval in the ice-

589 core records for the LIG suggested by this proxy. The published reconstructed temperatures for
590 GISP2 (blue symbols on upper panel)^{66,73} and NEEM (dark blue line on lower panel)⁶⁵ are based
591 on the relation $d\delta^{18}\text{O}_{\text{ice}}/dT = \sim 0.5\text{‰ C}^{-1}$ which is derived from Greenland ice-core sites
592 elsewhere⁷⁴. During the LIG, the precipitation-weighted $\delta^{18}\text{O}$ is likely biased to summer months
593 rather than mean annual temperature (van de Berg et al., 2013), so we compare this reconstruction
594 with our simulated summer temperature (JJA) (grey line on each panel). This suggests that our
595 simulated JJA temperatures are underestimating the mean of the reconstructions by 4-5°C. This
596 difference is reduced when we account for our simulated ice-surface lowering of ~200 m at NEEM
597 and ~400 m at GISP2 (see Fig. 3C) and assume the lapse rate of 7.5°C km⁻¹ used by Dahl-Jensen
598 et al.⁶⁵, thus placing our results within the published uncertainties of the reconstructions (green
599 line on each panel).

600 However, following the publication of Dahl-Jensen et al.⁶⁵, Masson-Delmotte et al.⁷⁵
601 established that the $d\delta^{18}\text{O}_{\text{ice}}/dT$ relation at the NEEM site is $\sim 1.1\text{‰ C}^{-1}$, suggesting that the NEEM
602 and GISP2 LIG summer temperatures are about half of the originally published values based on
603 the Vinther et al.⁷⁴ $d\delta^{18}\text{O}_{\text{ice}}/dT$ relation (red symbols on upper panel, red line on lower panel).
604 Masson-Delmotte et al.⁷⁵ (p. 1500) conclude that “For the last interglacial period, the observed
605 $\delta^{18}\text{O}$ anomaly of 3.6‰ at NEEM deposition site would then translate into 3.6 ± 0.7 °C warming,
606 instead of the estimate of 7.5 ± 1.8 °C (NEEM, 2013) that was obtained using the Greenland average
607 Holocene isotope–temperature relationship (Vinther et al., 2009).”

608 Our simulated JJA temperatures (grey line on each panel) are thus only 1-2°C colder than
609 the mean reconstructions for GISP2 and NEEM based on this new calibration, but they are in
610 excellent agreement with the mean values when accounting for our modeled ice-surface lowering
611 (green line on each panel).

612 Landais et al.⁷⁶ used $\delta^{15}\text{N}$ from the NEEM core to reconstruct temperatures that were 8.5°
613 $\pm 2.5^\circ\text{C}$ warmer during the LIG compared to preindustrial (PI). However, the $\delta^{15}\text{N}$ reconstruction
614 represents annual temperature whereas the $\delta^{18}\text{O}_{\text{ice}}$ temperatures are biased to the summer, which
615 is the critical season for influencing changes in surface mass balance through melting. The two
616 temperature reconstructions are thus not directly comparable. Moreover, Landais et al.⁷⁶ identify
617 “large uncertainties” (p. 1944) in their temperature reconstruction, including in the firn model
618 used, in the assumed accumulation rates, and in the potential influence of surface melt on firn
619 depth.

620 We thus conclude that when using the most suitable temperature calibration for the ice-
621 core sites and within the uncertainties of the ice-core proxy reconstructions, our climate model
622 successfully captures the LIG summer (JJA) temperature anomaly relative to pre-Industrial at
623 NEEM and GISP2. Consistent with this model-data agreement for warmer LIG JJA temperatures,
624 we find that the LIG surface mass balance of the GrIS is more negative than present day (Extended
625 Data Fig. 9).

626 Dahl-Jensen et al.⁶⁵ stated “during our NEEM field campaigns (2007-2012), the mean
627 surface air temperature in July reached -5.4°C .” However, Box⁷⁷ reported the average JJA
628 temperature for 2007-2012 at NEEM site as $-10.9 \pm 0.3^\circ\text{C}$, suggesting that Dahl-Jensen et al.⁶⁵ are
629 reporting a maximum July temperature value during their period of record rather than climatology.
630 But the JJA temperature that matters for comparing to the LIG is the pre-Industrial, which Box⁷⁷
631 found to be $-12.6 \pm 0.6^\circ\text{C}$ for 1840-1870 (period of record closest to pre-Industrial). (Dahl-Jensen
632 et al.⁶⁵ compared to the average of the last millennium.) Thus, even if the Dahl-Jensen et al.⁶⁵ LIG
633 temperature reconstruction is correct ($7.5 \pm 1.8^\circ\text{C}$ warmer than the mean of the past millennium),
634 average LIG summer temperatures would still be well below freezing ($\sim -5^\circ\text{C}$). More likely,

635 however, they are even further below freezing when using the $d\delta^{18}\text{O}_{\text{ice}}/dT$ relation established for
636 the NEEM site⁷⁵, i.e., 3.6 ± 0.7 °C warmer than the mean of the past millennium, with average LIG
637 summer temperatures thus being -9°C.

638 The evidence for surface melt at the NEEM ice core site is based on: (1) a low-resolution
639 record showing that out of 73 samples, seven have elevated CH₄ and N₂O during the interval 118-
640 127 ka, and (2) a high-resolution CH₄ record that suggests five melt events in the 123.5-122.5 ka
641 interval, or one every 200 years^{65,78}. Noble gases that were measured at the times of four of the
642 five elevated CH₄ events in the high-resolution record confirm melting at these times⁷⁸. This alone
643 makes it clear that these were infrequent periods of melting rather than continuous melting
644 throughout the LIG. According to Anais Orsi (personal communication, March, 2019), during a
645 melt event, such as the 2012 event⁷⁹, the melt percolates and refreezes in the top 1m of the firn,
646 often in many layers, so one melt event may be represented by more than one melt layer. Moreover,
647 although the noble gas results clearly identify four periods of enhanced melting, one cannot
648 exclude the possibility that each sample represents a single 2012-like melt event.

649 In summary, ice-core proxies suggest that Greenland LIG temperatures were warmer than
650 present, but constraining the amount of warming from these proxies remains uncertain. However,
651 even the highest estimates of warming still suggest that average JJA temperatures remained well
652 below freezing relative to pre-Industrial, and based on the more-appropriate $\delta^{18}\text{O}_{\text{ice}}$ -temperature
653 calibration from Masson-Delmotte et al.⁷⁵, are in good agreement with our simulated temperatures
654 for the ice-core sites. Consistent with this model-data agreement for warmer LIG JJA temperatures,
655 we find that the LIG surface mass balance of the GrIS is more negative than present day. Rare
656 episodes of melting occurred, but while their frequency may increase under higher mean
657 temperatures and insolation, such as is recorded in the Holocene section of the GISP2 ice core⁸⁰,

658 we conclude that with a frequency of perhaps only one melt event every 200 years, they had a
659 negligible influence on long-term surface mass balance, and average summer temperatures at the
660 NEEM site otherwise remained well below freezing during the LIG.

661 **Influence of freshwater forcing from modeled mass loss from the Greenland and Antarctic**
662 **Ice Sheets on ocean circulation during the last interglaciation.** We did not include additional
663 freshwater (FW) forcing after 129.5 ka, but we show here that the FW fluxes from our modeled
664 mass loss from the Greenland and Antarctic ice sheets (GrIS and AIS) after 129.5 ka (during the
665 LIG) were too small to have influenced the Atlantic Meridional Overturning Circulation (AMOC)
666 or Antarctic Bottom Water (AABW) formation. Since global sea level reached modern at 129-130
667 ka, and our modeled AMOC resumes at 129.5 ka, we only consider the FW fluxes from the GrIS
668 and AIS since 129.5 ka.

669 From 129.5 to 127 ka, modeled GrIS mass loss was 0.2 m of sea-level equivalent, which
670 is equivalent to a FW flux of 0.0009 Sv. From 127 ka to 117.5 ka, GrIS mass loss was 0.09 m,
671 which is equivalent to 0.0001 Sv. For reference, Bakker et al.⁸¹ showed that a FW flux of 0.01 Sv
672 from Greenland for the RCP4.5 scenario (see their Fig. SI3) results in a median reduction in the
673 AMOC of ~5% (their Fig. 2, GrIS only). The FW fluxes from LIG loss of the GrIS in our model
674 are two orders of magnitude smaller than this, and thus would have no impact on the AMOC, and
675 thus on our ice-sheet model simulations.

676 From 129.5ka to 123.5 ka, AIS mass loss was 4.1 m, which is equivalent to a FW flux of
677 0.008 Sv. Bakker et al.⁸² found that a FW flux of 0.12 Sv from the AIS increases variability in
678 AABW by ~10% and in AMOC by ~5%. The FW fluxes from LIG loss of the AIS in our model
679 is a factor of 15 smaller than this, and thus would have no impact on AABW or the AMOC, and
680 thus on our ice-sheet model simulations.

681 **Code availability.**682 CCSM3 is freely available as open-source code from <http://www.cesm.ucar.edu/models/ccsm3.0/>683 PISM is freely available as open-source code from <https://github.com/pism/pism.git>.684 **Data availability**

685 Antarctic bedrock topography and ice thickness data are from the BEDMAP2 compilation,

686 available at <https://secure.antarctica.ac.uk/data/bedmap2/>. Greenland topography and ice thickness687 data are from BedMachine v3, available at <https://nsidc.org/data/idbmg4>. Greenland mass balance

688 and geothermal heat flux data are available from the seaRISE website:

689 <http://websrv.cs.umt.edu/isis/index.php/Data>. Information on Antarctic surface mass balance data690 are available at <http://www.projects.science.uu.nl/iceclimate/models/antarctica.php#racmo23>.

691 Antarctic geothermal heat flux data are available at the Open Science Framework

692 <https://doi.pangaea.de/10.1594/PANGAEA.882503>. The datasets generated and used for this

693 study (Figs. 1,2,3,4, Extended Data Figs. 3,4,5,6,7,8,9) are available from the Open Science

694 Framework (DOI 10.17605/OSF.IO/FX7WK).

695

696

697 30 Yeager, S. G., Shields, C. A., Large, W. G. & Hack, J. J. The low-resolution CCSM3.
698 *Journal of Climate* **19**, 2545-2566, doi:10.1175/Jcli3744.1 (2006).699 31 He, F. *Simulating transient climate evolution of the last deglaciation with CCSM3* Ph.D.
700 thesis, The University of Wisconsin - Madison, (2011).701 32 Luthi, D. *et al.* High-resolution carbon dioxide concentration record 650,000-800,000
702 years before present. *Nature* **453**, 379-382, doi:10.1038/nature06949 (2008).703 33 Peltier, W. R. Global glacial isostasy and the surface of the ice-age earth: The ice-5G
704 (VM2) model and grace. *Annual Review of Earth and Planetary Sciences* **32**, 111-149
705 (2004).706 34 Grant, K. M. *et al.* Rapid coupling between ice volume and polar temperature over the
707 past 150,000 years. *Nature* **491**, 744-747, doi:10.1038/nature11593 (2012).708 35 Aschwanden, A., Fahnestock, M. A. & Truffer, M. Complex greenland outlet glacier
709 flow captured. *Nature Communications* **7**, doi:10.1038/ncomms10524 (2016).710 36 Golledge, N. R. *et al.* The multi-millennial Antarctic commitment to future sea-level rise.
711 *Nature* **526**, 421-+, doi:10.1038/nature15706 (2015).

- 712 37 Schoof, C. A variational approach to ice stream flow. *Journal of Fluid Mechanics* **556**,
713 227-251, doi:Doi 10.1017/S0022112006009591 (2006).
- 714 38 Bueler, E. & Brown, J. Shallow shelf approximation as a "sliding law" in a
715 thermomechanically coupled ice sheet model. *Journal of Geophysical Research-Earth*
716 *Surface* **114**, F03008 (2009).
- 717 39 Van Pelt, W. J. J. & Oerlemans, J. Numerical simulations of cyclic behaviour in the
718 Parallel Ice Sheet Model (PISM). *Journal of Glaciology* **58**, 347-360,
719 doi:10.3189/2012JoG11J217 (2012).
- 720 40 Feldmann, J., Albrecht, T., Khroulev, C., Pattyn, F. & Levermann, A. Resolution-
721 dependent performance of grounding line motion in a shallow model compared with a
722 full-Stokes model according to the MIS3d intercomparison. *Journal of Glaciology*
723 **60**, 353-360, doi:10.3189/2014JoG13J093 (2014).
- 724 41 Levermann, A. *et al.* Kinematic first-order calving law implies potential for abrupt ice-
725 shelf retreat. *Cryosphere* **6**, 273-286, doi:10.5194/tc-6-273-2012 (2012).
- 726 42 Fausto, R. S., Ahlstrom, A. P., Van As, D., Boggild, C. E. & Johnsen, S. J. A new
727 present-day temperature parameterization for Greenland. *Journal of Glaciology* **55**, 95-
728 105, doi:Doi 10.3189/002214309788608985 (2009).
- 729 43 van Wessem, J. M. *et al.* Improved representation of East Antarctic surface mass balance
730 in a regional atmospheric climate model. *Journal of Glaciology* **60**, 761-770,
731 doi:10.3189/2014JoG14J051 (2014).
- 732 44 Golledge, N. R. *et al.* Antarctic climate and ice-sheet configuration during the early
733 Pliocene interglacial at 4.23 Ma. *Climate of the Past* **13**, 959-975, doi:10.5194/cp-13-
734 959-2017 (2017).
- 735 45 Munneke, P. K. *et al.* A new albedo parameterization for use in climate models over the
736 Antarctic ice sheet. *Journal of Geophysical Research-Atmospheres* **116**,
737 doi:10.1029/2010jd015113 (2011).
- 738 46 van den Broeke, M., C. Bus, C., Ettema, J. & P. Smeets, P. Temperature thresholds for
739 degree-day modelling of Greenland ice sheet melt rates. *Geophysical Research Letters*
740 **37**, L18501, doi:10.1029/2010GL044123 (2010).
- 741 47 Plach, A. *et al.* Eemian Greenland SMB strongly sensitive to model choice. *Climate of*
742 *the Past* **14**, 1463-1485, doi:10.5194/cp-14-1463-2018 (2018).
- 743 48 Hellmer, H. H. & Olbers, D. J. A 2-Dimensional Model for the Thermohaline Circulation
744 under an Ice Shelf. *Antarctic Science* **1**, 325-336 (1989).
- 745 49 Bernales, J., Rogozhina, I. & Thomas, M. Melting and freezing under Antarctic ice
746 shelves from a combination of ice-sheet modelling and observations. *Journal of*
747 *Glaciology* **63**, 731-744, doi:10.1017/jog.2017.42 (2017).
- 748 50 Morlighem, M. *et al.* BedMachine v3: Complete Bed Topography and Ocean Bathymetry
749 Mapping of Greenland From Multibeam Echo Sounding Combined With Mass
750 Conservation. *Geophysical Research Letters* **44**, 11051-11061,
751 doi:10.1002/2017gl074954 (2017).
- 752 51 Fretwell, P. *et al.* Bedmap2: improved ice bed, surface and thickness datasets for
753 Antarctica. *Cryosphere* **7**, 375-393, doi:10.5194/tc-7-375-2013 (2013).
- 754 52 Mackintosh, A. *et al.* Retreat of the East Antarctic ice sheet during the last glacial
755 termination. *Nature Geoscience* **4**, 195-202, doi:10.1038/NGEO1061 (2011).

- 756 53 Briggs, R., Pollard, D. & Tarasov, L. A glacial systems model configured for large
757 ensemble analysis of Antarctic deglaciation. *Cryosphere* **7**, 1949-1970, doi:10.5194/tc-7-
758 1949-2013 (2013).
- 759 54 Gollledge, N. R., Fogwill, C. J., Mackintosh, A. N. & Buckley, K. M. Dynamics of the
760 last glacial maximum Antarctic ice-sheet and its response to ocean forcing. *Proceedings*
761 *of the National Academy of Sciences of the United States of America* **109**, 16052-16056,
762 doi:10.1073/pnas.1205385109 (2012).
- 763 55 Gollledge, N. R. *et al.* Antarctic contribution to meltwater pulse 1A from reduced
764 Southern Ocean overturning. *Nature Communications* **5** (2014).
- 765 56 Weber, M. E. *et al.* Millennial-scale variability in Antarctic ice-sheet discharge during the
766 last deglaciation. *Nature* **510**, 134+, doi:Doi 10.1038/Nature13397 (2014).
- 767 57 Simpson, M. J. R., Milne, G. A., Huybrechts, P. & Long, A. J. Calibrating a glaciological
768 model of the Greenland ice sheet from the Last Glacial Maximum to present-day using
769 field observations of relative sea level and ice extent. *Quaternary Science Reviews* **28**,
770 1631-1657, doi:10.1016/j.quascirev.2009.03.004 (2009).
- 771 58 Lecavalier, B. S. *et al.* A model of Greenland ice sheet deglaciation constrained by
772 observations of relative sea level and ice extent. *Quaternary Science Reviews* **102**, 54-84,
773 doi:Doi 10.1016/J.Quascirev.2014.07.018 (2014).
- 774 59 Stone, E. J., Lunt, D. J., Annan, J. D. & Hargreaves, J. C. Quantification of the Greenland
775 ice sheet contribution to Last Interglacial sea level rise. *Climate of the Past* **9**, 621-639,
776 doi:10.5194/cp-9-621-2013 (2013).
- 777 60 Goelzer, H., Huybrechts, P., Loutre, M. F. & Fichefet, T. Last Interglacial climate and
778 sea-level evolution from a coupled ice sheet-climate model. *Climate of the Past* **12**, 2195-
779 2213, doi:10.5194/cp-12-2195-2016 (2016).
- 780 61 Mitrovica, J. X., Wahr, J., Matsuyama, I. & Paulson, A. The rotational stability of an ice-
781 age earth. *Geophysical Journal International* **161**, 491-506 (2005).
- 782 62 Dziewonski, A. M. & Anderson, D. L. Preliminary reference Earth model. *Physics of the*
783 *Earth and Planetary Interiors* **25**, 297-356 (1981).
- 784 63 Peltier, W. R., Argus, D. F. & Drummond, R. Space geodesy constrains ice age terminal
785 deglaciation: The global ICE-6G_C (VM5a) model. *Journal of Geophysical Research-*
786 *Solid Earth* **120**, 450-487, doi:10.1002/2014jb011176 (2015).
- 787 64 Shakun, J. D., Lea, D. W., Lisiecki, L. E. & Raymo, M. E. An 800-kyr record of global
788 surface ocean delta O-18 and implications for ice volume-temperature coupling. *Earth*
789 *and Planetary Science Letters* **426**, 58-68, doi:10.1016/j.epsl.2015.05.042 (2015).
- 790 65 Dahl-Jensen, D. *et al.* Eemian interglacial reconstructed from a Greenland folded ice
791 core. *Nature* **493**, 489-494 (2013).
- 792 66 Yau, A., Bender, M. L., Robinson, A. & Brook, E. J. Reconstructing the last interglacial
793 at Summit, Greenland: Insights from GISP2. *Proceedings of the National Academy of*
794 *Sciences* **113**, 9710-9715, doi:10.1073/pnas.1524766113 (2016).
- 795 67 Liu, Z. Y. *et al.* Younger Dryas cooling and the Greenland climate response to CO₂.
796 *Proceedings of the National Academy of Sciences of the United States of America* **109**,
797 11101-11104, doi:10.1073/pnas.1202183109 (2012).
- 798 68 van de Berg, W. J., van den Broeke, M. R., van Meijgaard, E. & Kaspar, F. Importance of
799 precipitation seasonality for the interpretation of Eemian ice core isotope records from
800 Greenland. *Climate of the Past* **9**, 1589-1600, doi:10.5194/cp-9-1589-2013 (2013).

- 801 69 Sime, L. C. *et al.* Warm climate isotopic simulations: what do we learn about interglacial
802 signals in Greenland ice cores? *Quaternary Science Reviews* **67**, 59-80,
803 doi:10.1016/j.quascirev.2013.01.009 (2013).
- 804 70 Buizert, C. *et al.* Greenland temperature response to climate forcing during the last
805 deglaciation. *Science* **345**, 1177-1180, doi:10.1126/science.1254961 (2014).
- 806 71 Rhines, A. & Huybers, P. J. Sea Ice and Dynamical Controls on Preindustrial and Last
807 Glacial Maximum Accumulation in Central Greenland. *Journal of Climate* **27**, 8902-
808 8917, doi:10.1175/JCLI-D-14-00075.1 (2014).
- 809 72 Pedersen, R. A., Langen, P. L. & Vinther, B. M. Greenland during the last interglacial:
810 the relative importance of insolation and oceanic changes. *Climate of the Past* **12**, 1907-
811 1918, doi:10.5194/cp-12-1907-2016 (2016).
- 812 73 Suwa, M., von Fischer, J. C., Bender, M. L., Landais, A. & Brook, E. J. Chronology
813 reconstruction for the disturbed bottom section of the GISP2 and the GRIP ice cores:
814 Implications for Termination II in Greenland. *Journal of Geophysical Research-*
815 *Atmospheres* **111**, -, doi:10.1029/2005jd006032 (2006).
- 816 74 Vinther, B. M. *et al.* Holocene thinning of the Greenland ice sheet. *Nature* **461**, 385-388,
817 doi:10.1038/nature08355 (2009).
- 818 75 Masson-Delmotte, V. *et al.* Recent changes in north-west Greenland climate documented
819 by NEEM shallow ice core data and simulations, and implications for past-temperature
820 reconstructions. *The Cryosphere* **9**, 1481-1504 (2015).
- 821 76 Landais, A. *et al.* How warm was Greenland during the last interglacial period? *Climate*
822 *of the Past* **12**, 1933-1948, doi:10.5194/cp-12-1933-2016 (2016).
- 823 77 Box, J. E. Greenland Ice Sheet Mass Balance Reconstruction. Part II: Surface Mass
824 Balance (1840-2010). *Journal of Climate* **26**, 6974-6989, doi:10.1175/JCLI-D-12-
825 00518.1 (2013).
- 826 78 Orsi, A. J. *et al.* Differentiating bubble-free layers from melt layers in ice cores using
827 noble gases. *Journal of Glaciology* **61**, 585-594, doi:10.3189/2015JoG14J237 (2015).
- 828 79 Tedesco, M. *et al.* Evidence and analysis of 2012 Greenland records from spaceborne
829 observations, a regional climate model and reanalysis data. *Cryosphere* **7**, 615-630,
830 doi:10.5194/tc-7-615-2013 (2013).
- 831 80 Alley, R. B. & Anandakrishnan, A. Variations in melt-layer frequency in the GISP2 ice
832 core: implications for Holocene summer temperatures in central Greenland. *Annals of*
833 *Glaciology* **21**, 64-70 (1995).
- 834 81 Bakker, P. *et al.* Fate of the Atlantic Meridional Overturning Circulation: Strong decline
835 under continued warming and Greenland melting. *Geophysical Research Letters* **43**,
836 12252-12260, doi:10.1002/2016GL070457 (2016).
- 837 82 Bakker, P., Clark, P. U., Gollledge, N. R., Schmittner, A. & Weber, M. E. Centennial-
838 scale Holocene climate variations amplified by Antarctic Ice Sheet discharge. *Nature*
839 **541**, 72-+, doi:10.1038/nature20582 (2017).
- 840 83 Deaney, E. L., Barker, S. & van de Flierdt, T. Timing and nature of AMOC recovery
841 across Termination 2 and magnitude of deglacial CO₂ change. *Nature Communications*
842 **8**, doi:10.1038/ncomms14595 (2017).
- 843 84 Bazin, L. *et al.* An optimized multi-proxy, multi-site Antarctic ice and gas orbital
844 chronology (AICC2012): 120-800 ka. *Climate of the Past* **9**, 1715-1731, doi:10.5194/cp-
845 9-1715-2013 (2013).

- 846 85 Oppo, D. W., McManus, J. F. & Cullen, J. L. Evolution and demise of the Last
847 Interglacial warmth in the subpolar North Atlantic. *Quaternary Science Reviews* **25**,
848 3268-3277, doi:10.1016/j.quascirev.2006.07.006 (2006).
- 849 86 Skinner, L. C. & Shackleton, N. J. Deconstructing Terminations I and II: revisiting the
850 glacioeustatic paradigm based on deep-water temperature estimates. *Quaternary Science*
851 *Reviews* **25**, 3312-3321, doi:10.1016/j.quascirev.2006.07.005 (2006).
- 852 87 Goni, M. F. S. *et al.* European climate optimum and enhanced Greenland melt during the
853 Last Interglacial. *Geology* **40**, 627-630, doi:10.1130/G32908.1 (2012).
- 854 88 Roberts, N. L., Piotrowski, A. M., McManus, J. F. & Keigwin, L. D. Synchronous
855 deglacial overturning and water mass source changes. *Science* **327**, 75-78,
856 doi:10.1126/science.1178068 (2010).
- 857 89 McManus, J. F., Francois, R., Gherardi, J. M., Keigwin, L. D. & Brown-Leger, S.
858 Collapse and rapid resumption of Atlantic meridional circulation linked to deglacial
859 climate changes. *Nature* **428**, 834-837, doi:10.1038/nature02494 (2004).
- 860 90 Stern, J. V. & Lisiecki, L. E. North Atlantic circulation and reservoir age changes over
861 the past 41,000years. *Geophysical Research Letters* **40**, 3693-3697,
862 doi:10.1002/grl.50679 (2013).
- 863 91 Menviel, L. *et al.* The penultimate deglaciation: protocol for PMIP4 transient numerical
864 simulations between 140 and 127 ka. *Climate of the Past Discussions*,
865 doi:doi.org/10.5194/cp-2018-106 (2018).
- 866 92 Thomas, A. L. *et al.* Penultimate Deglacial Sea-Level Timing from Uranium/Thorium
867 Dating of Tahitian Corals. *Science* **324**, 1186-1189, doi:10.1126/science.1168754 (2009).
- 868 93 Esat, T. M., McCulloch, M. T., Chappell, J., Pillans, B. & Omura, A. Rapid fluctuations
869 in sea level recorded at Huon Peninsula during the penultimate deglaciation. *Science* **283**,
870 197-201, doi:DOI 10.1126/science.283.5399.197 (1999).
- 871 94 Cheng, H. *et al.* Improvements in Th-230 dating, Th-230 and U-234 half-life values, and
872 U-Th isotopic measurements by multi-collector inductively coupled plasma mass
873 spectrometry. *Earth and Planetary Science Letters* **371**, 82-91,
874 doi:10.1016/j.epsl.2013.04.006 (2013).
- 875 95 Peak, B. A., Mitrovica, J. X., Latychev, K., Powell, E. & Lau, H. C. P. Complex earth
876 structure and glacial isostatic adjustment in the Red Sea. *American Geophysical Union*,
877 PP13C-1343 (2018).
- 878 96 Lambeck, K. *et al.* Sea level and shoreline reconstructions for the Red Sea: isostatic and
879 tectonic considerations and implications for hominin migration out of Africa. *Quaternary*
880 *Science Reviews* **30**, 3542-3574 (2011).
- 881 97 Lambeck, K., Rouby, H., Purcell, A., Sun, Y. & Sambridge, M. Sea level and global ice
882 volumes from the Last Glacial Maximum to the Holocene. *Proceedings of the National*
883 *Academy of Sciences* **111**, 15296-15303 (2014).

884
885

886

887

888 **Extended Data Fig. 1. Climate and sea-level records for Termination II and Termination I.**

889 **(a)** ϵ Nd records from the North Atlantic Ocean as proxies of Atlantic meridional overturning
 890 circulation (AMOC)^{16,83}. **(b)** CCSM3 maximum AMOC transport (below 500 m) (this study). **(c)**
 891 EPICA Dome C δ D record on AICC2012 age model as proxy of Antarctic temperature⁸⁴ (blue
 892 line) and percentage of warm planktonic foraminiferal species as proxy of North Atlantic sea
 893 surface temperatures⁸³ (grey line). **(d)** δ^{18} O record from Chinese stalagmite as proxy of Asian
 894 monsoon strength¹⁸. **(e)** Rate of sea-level change derived from a relative sea level (RSL)
 895 reconstruction based on benthic foraminifera isotopes¹. **(f)** A stack of North Atlantic ice-rafted
 896 debris records recording Heinrich event 11 (H11)^{83,85-87}. **(g)** ϵ Nd⁸⁸ (brown, orange symbols) and
 897 Pa/Th⁸⁹ (purple, green symbols, 1 sigma uncertainty) records from the North Atlantic Ocean as
 898 proxies of AMOC. **(h)** CCSM3 maximum AMOC transport (below 500 m) (this study). **(i)** EPICA
 899 Dome C δ D record on AICC2012 age model (dark blue line)⁸⁴ as proxy of Antarctic temperature
 900 and temperature reconstruction from the Greenland GISP2 ice core (light blue line)⁷⁰. **(j)** δ^{18} O
 901 record from Chinese stalagmite as proxy of Asian monsoon strength¹⁸. **(k)** Rate of sea-level change
 902 derived from a RSL reconstruction based on benthic foraminifera isotopes¹. **(l)** A stack of North
 903 Atlantic ice-rafted debris records recording Heinrich event 1 (H1)⁹⁰.

904

905 **Extended Data Fig. 2. Sea-level records for the last two terminations and interglaciations. (a)**

906 Sea-level reconstructions for the penultimate deglaciation and the last interglaciation (the latter
 907 identified by the grey-shaded area). Eustatic sea-level record is based on benthic foraminifera
 908 isotopes (blue line with 1 σ uncertainty)¹ and relative sea-level (RSL) record is based on Red Sea
 909 isotopes (gray crosses; green line, 1-kyr moving Gaussian filter)³⁴ placed on a revised age model⁹¹.
 910 Also shown are RSL data from U-series dated corals at Tahiti (sky blue circles)⁹², Huon Peninsula

911 (light blue green circle; altered samples shown by gray circles)⁹³, the Seychelles (light green
912 circles)²⁵, western Australia (blue circles)²⁴, and the Bahamas (cyan circles)²⁴. All of the U-series
913 ages have been recalculated to normalize them with the same set of decay constants for ²³⁴U and
914 ²³⁰Th⁹⁴ and are shown with 2 σ age uncertainty. We note that the offset between the Red Sea record
915 (green line) and the benthic foraminifera record (blue line) may reflect the complex 3-dimensional
916 Earth structure in the vicinity of the Red Sea rift^{95,96}. The variability in the Red Sea and Huon
917 Peninsula RSL records may reflect a sea-level reversal at ~137 ka⁹¹ which, if it existed, was too
918 small to be recorded by the benthic foraminiferal record. The rate of sea-level change based on the
919 benthic foraminiferal record is also shown. **(b)** Sea-level reconstructions for the last deglaciation
920 and the present interglaciation (the latter identified by the grey-shaded area). The record of global
921 mean sea level is based on benthic foraminifera isotopes (blue line with 1 σ uncertainty)¹. Also
922 shown are individual sea-level estimates (black circles, 2 σ uncertainty) that have been corrected
923 for glacial isostatic adjustment⁹⁷. Rate of sea-level change based on the benthic foraminiferal
924 record is also shown. **(c)** Upper panel shows eustatic sea-level reconstructions for the penultimate
925 deglaciation (blue line with 1 σ uncertainty) and the last deglaciation (black line with 1 σ
926 uncertainty)¹. Lower panel shows June 21 insolation for 65°N for the penultimate deglaciation
927 (blue line) and the last deglaciation (black line)⁷.

928

929 **Extended Data Fig. 3. Comparison of our freshwater forcing during T-II with other**
930 **estimates. (a)** Our simulated changes in AMOC. **(b)** Our FW forcing. **(c)** Reconstruction of
931 freshwater (FW) flux from sea-level reconstructions from Waelbroeck et al.¹. **(d)** Reconstruction
932 of FW flux from sea-level reconstructions from Marino et al.³ **(e)** Our stack of ice-rafted for
933 Heinrich event 11 (H11) (Extended Data Fig. 1), which shows that the H11 interval of iceberg

934 discharge is in good agreement with the timing of our FW forcing. (f) The sea-level change
935 associated with our FW flux into the North Atlantic (grey line), the sea-level change associated
936 with the ICE-5G ice sheets³³ used as a boundary condition in our climate model (green line), and
937 a reconstruction of global sea-level change¹ (blue line with 1 sigma uncertainty). The timing of
938 sea-level change in the ICE-5G time series shown here was adjusted from its chronology for T-I
939 by adjusting the corresponding sea-level rise to closely follow the Waelbroeck et al.¹ and Grant et
940 al.³⁴ sea-level reconstructions for the penultimate deglaciation.

941

942 **Extended Data Fig. 4. Maps of the evolution of temperature at 400-m water depth in the**
943 **North Atlantic, Arctic, and Southern Oceans between 138 ka and 124 ka relative to**
944 **temperature at 140 ka. a-h**, Maps of the evolution of temperature at 400-m water depth in the
945 North Atlantic and Arctic Oceans for (a) 138-140 ka, (b) 136-140 ka, (c) 134-140 ka, (d) 132-
946 140 ka, (e) 130-140 ka, (f) 128-140 ka, (g) 126-140 ka, and (h) 124-140 ka. **i-p**, Maps of the
947 evolution of temperature at 400-m water depth in the Southern Ocean for (i) 138-140 ka, (j) 136-
948 140 ka, (k) 134-140 ka, (l) 132-140 ka, (m) 130-140 ka, (n) 128-140 ka, (o) 126-140 ka, and (p)
949 124-140 ka.

950

951 **Extended Data Fig. 5. Predicted topography for the area covered by the Scandinavian Ice**
952 **Sheet at 131 ka.** The calculation is based on the LAM ice history (see text) and an Earth model
953 characterized by a lithosphere of thickness 100 km, upper mantle viscosity of 3×10^{20} Pa s, and
954 lower mantle viscosity of 5×10^{22} Pa s. The white zone in (a) represents coverage of grounded
955 ice extent at this time and the dashed white line on this frame is the shoreline location. Frame (b)
956 is identical to (a), except the area of ice coverage is removed. It is clear from frame (a) that all

957 but the southeast section of the perimeter of the Scandinavian ice sheet is predicted to be marine
958 based at this time, and from frame (b) that much of the interior of the ice sheet was also marine
959 based.

960

961 **Extended Data Fig. 6. Results of sensitivity tests to oceanic forcing of the Greenland and**

962 **Antarctic ice sheets. (a)** Response of Greenland Ice Sheet to atmospheric forcing from CCSM3

963 with fixed ocean temperatures for the Penultimate Glacial Maximum (PGM) (blue line) and for

964 the Last Interglaciation (LIG) (orange line) compared to ice-sheet response to atmospheric and

965 oceanic forcing (black line). Present interglacial ice volume shown by horizontal dashed line. (b)

966 Response of Antarctic Ice Sheet to atmospheric forcing from CCSM3 with fixed ocean

967 temperatures for the PGM (blue line) and for the LIG (orange line) compared to ice-sheet response

968 to atmospheric and oceanic forcing (black line). Present interglacial ice volume shown by

969 horizontal dashed line. (c) As in a, response of Greenland Ice Sheet to atmospheric forcing from

970 CCSM3 with fixed ocean temperatures for the LIG (orange line), but the vertical scale (grounded

971 ice volume) has been increased to better illustrate the response. The initial ice-sheet size used in

972 this experiment (and the comparable one for Antarctica) was the LIG ice sheet, whereas the climate

973 forcing used was for the penultimate deglaciation and the LIG, i.e., from colder-than-present to

974 LIG climate, resulting in a small response to the atmospheric forcing, since the LIG ice-sheet size

975 had already adjusted to the combined atmospheric and oceanic forcing, as shown by the black line

976 in a.

977

978 **Extended Data Fig. 7. Predictions of relative sea level (RSL) at three far-field sites (the**

979 **Seychelles, Western Australia, and Mallorca) and one intermediate-field site (Bahamas). a-**

980 **d**, RSL predictions for the Bahamas from the full suite of simulations that bound from above all
981 coral data with the exception of the earliest datum (at ~131 ka) for **(a)** the COL ice history, **(b)** the
982 LAM ice history, **(c)** the HYB ice history, and **(d)** the WAE ice history. Age uncertainty is 2σ , and
983 depth uncertainty reflects uncertainty in habitat depth. **e-h**, RSL predictions for the Seychelles
984 from the full suite of simulations that lie above the three coral records with an elevation of ~4 m
985 for **(e)** the COL ice history, **(f)** the LAM ice history, **(g)** the HYB ice history, and **(h)** the WAE ice
986 history. Age uncertainty is 2σ , and depth uncertainty reflects uncertainty in habitat depth. **i-l**, RSL
987 predictions for western Australia from the full suite of simulations that bound from above all coral
988 data for **(i)** the COL ice history, **(j)** the LAM ice history, **(k)** the HYB ice history, and **(l)** the WAE
989 ice history. Age uncertainty is 2σ , and depth uncertainty reflects uncertainty in habitat depth. **m-**
990 **p**, RSL predictions for Mallorca from the full suite of simulations that fit the data within 50% of
991 the minimum misfit achieved for all simulations for **(m)** the COL ice history, **(n)** the LAM ice
992 history, **(o)** the HYB ice history, and **(p)** the WAE ice history. Age uncertainty is 2σ , and depth
993 uncertainty reflects uncertainty in speleothem water depth.

994

995 **Extended Data Fig. 8. Sensitivity of Greenland ice sheet model to melt parameterisation. (a)**
996 Time series of tuning experiments for the Greenland Ice Sheet with the preferred run in blue and
997 three runs used for **b-d** shown in green, orange, and red. **b-d**. Surface elevation differences under
998 a present-day climatology at the end of the 40,000-year T-I parameter tuning experiments, using
999 degree-day factors drawn from our ensemble that **(b)**, give a low amount of surface melting, **(c)**,
1000 medium amount of surface melting, and **(d)**, high amount of surface melting. Values shown are
1001 differences from the reference experiment. These experiments are identical to the T-I reference
1002 experiment used to parameterise the T-II simulations (Fig. 3) except for the degree-day factors

1003 used. The results show that our ice-sheet model is sensitive to the way in which surface mass
1004 balance is parameterised by controlling the amount of surface melting.

1005
1006 **Extended Data Fig. 9. Simulated ice-volume changes and components of the mass balance**
1007 **for the Greenland Ice Sheet. (a)** Simulated changes in ice volume for T-I. **(b)** Simulated changes
1008 in mass-balance components for T-I. **(c)** Simulated changes in ice volume for T-II. **(d)** Simulated
1009 changes in mass-balance components for T-II. **(e)** Modelled surface mass balance anomaly during
1010 the Last Interglaciation (129-120 ka) with respect to modelled present day.

1011
1012 **Extended Data Fig. 10. Comparison of our simulated summer temperature for Greenland**
1013 **ice-core sites with the temperature reconstructions for these sites based on $\delta^{18}\text{O}_{\text{ice}}$.** **(a)** The
1014 simulated summer temperature (JJA) (grey line) and lapse-rate corrected JJA temperature (green
1015 line) compared to reconstructed temperatures for the GISP2 ice-core site (blue symbols, 1 sigma
1016 uncertainty)^{66,73} based on the relation $d\delta^{18}\text{O}_{\text{ice}}/dT = \sim 0.5\% \text{ C}^{-1}$ which is derived from Greenland
1017 ice-core sites elsewhere⁷⁴. Also shown are the reconstructed temperatures using the $d\delta^{18}\text{O}_{\text{ice}}/dT$
1018 relation established for the NEEM site ($\sim 1.1\% \text{ C}^{-1}$)⁷⁵ (red symbols, 1 sigma uncertainty),
1019 suggesting that the GISP2 LIG summer temperatures are about half of the originally published
1020 values based on the Vinther et al.⁷⁴ $d\delta^{18}\text{O}_{\text{ice}}/dT$ relation and in good agreement with our model
1021 results. **(b)** The simulated JJA temperature (grey line) and lapse-rate corrected JJA temperature
1022 (green line) compared to reconstructed temperatures for the NEEM ice-core site (dark blue line,
1023 gray shading is uncertainty)⁶⁵ based on the relation $d\delta^{18}\text{O}_{\text{ice}}/dT = \sim 0.5\% \text{ C}^{-1}$ which is derived from
1024 Greenland ice-core sites elsewhere⁷⁴. Also shown are the reconstructed temperatures using the
1025 $d\delta^{18}\text{O}_{\text{ice}}/dT$ relation established for the NEEM site ($\sim 1.1\% \text{ C}^{-1}$)⁷⁵ (red line, pink shading is

1026 uncertainty), suggesting that the NEEM LIG summer temperatures are about half of the originally
1027 published values based on the Vinther et al.⁷⁴ $d\delta^{18}\text{O}_{\text{ice}}/dT$ relation and in good agreement with our
1028 model results. These reconstructions span the interval 127-120 ka, which is the warmest interval
1029 in the ice-core records for the LIG suggested by this proxy.

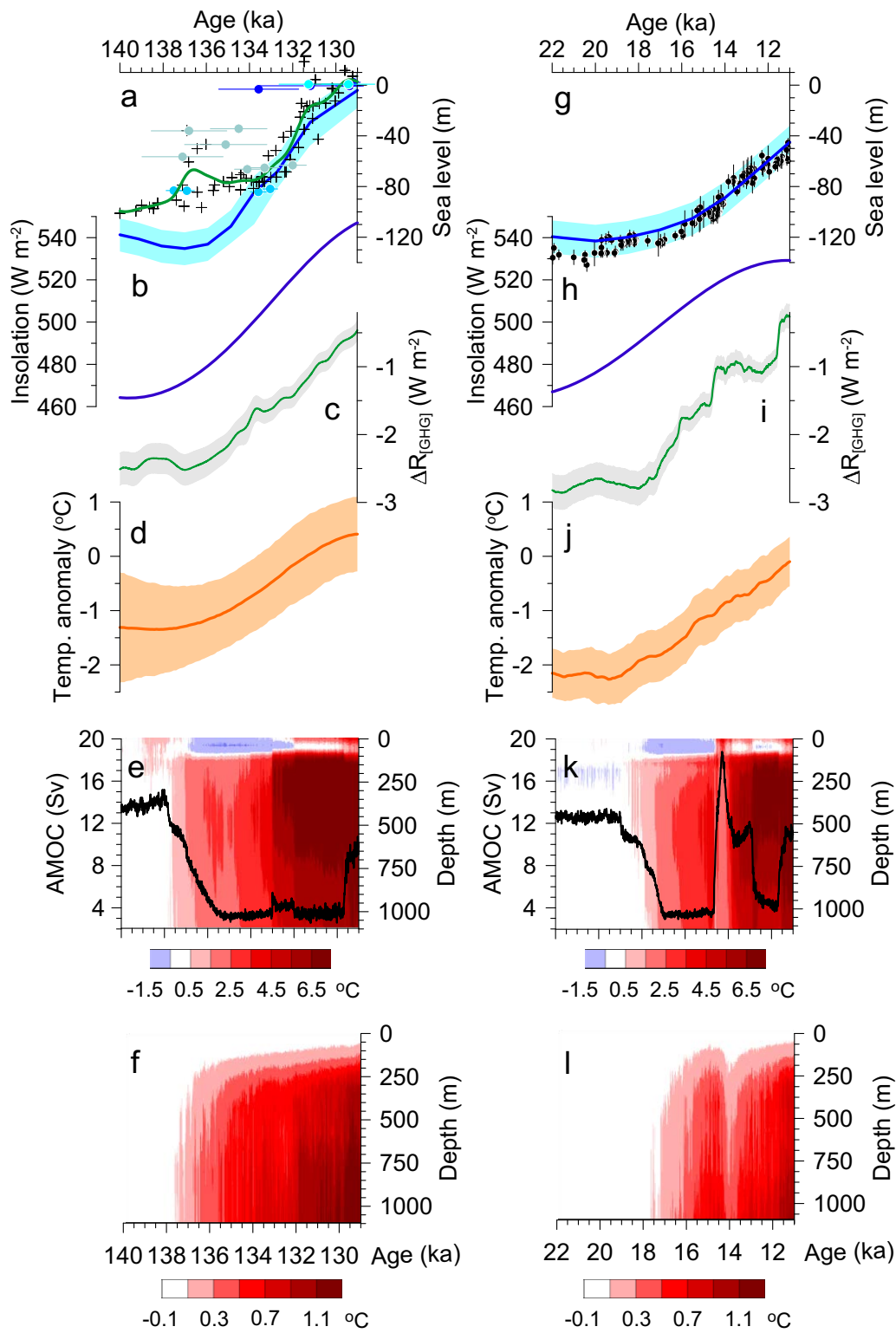


Figure 1

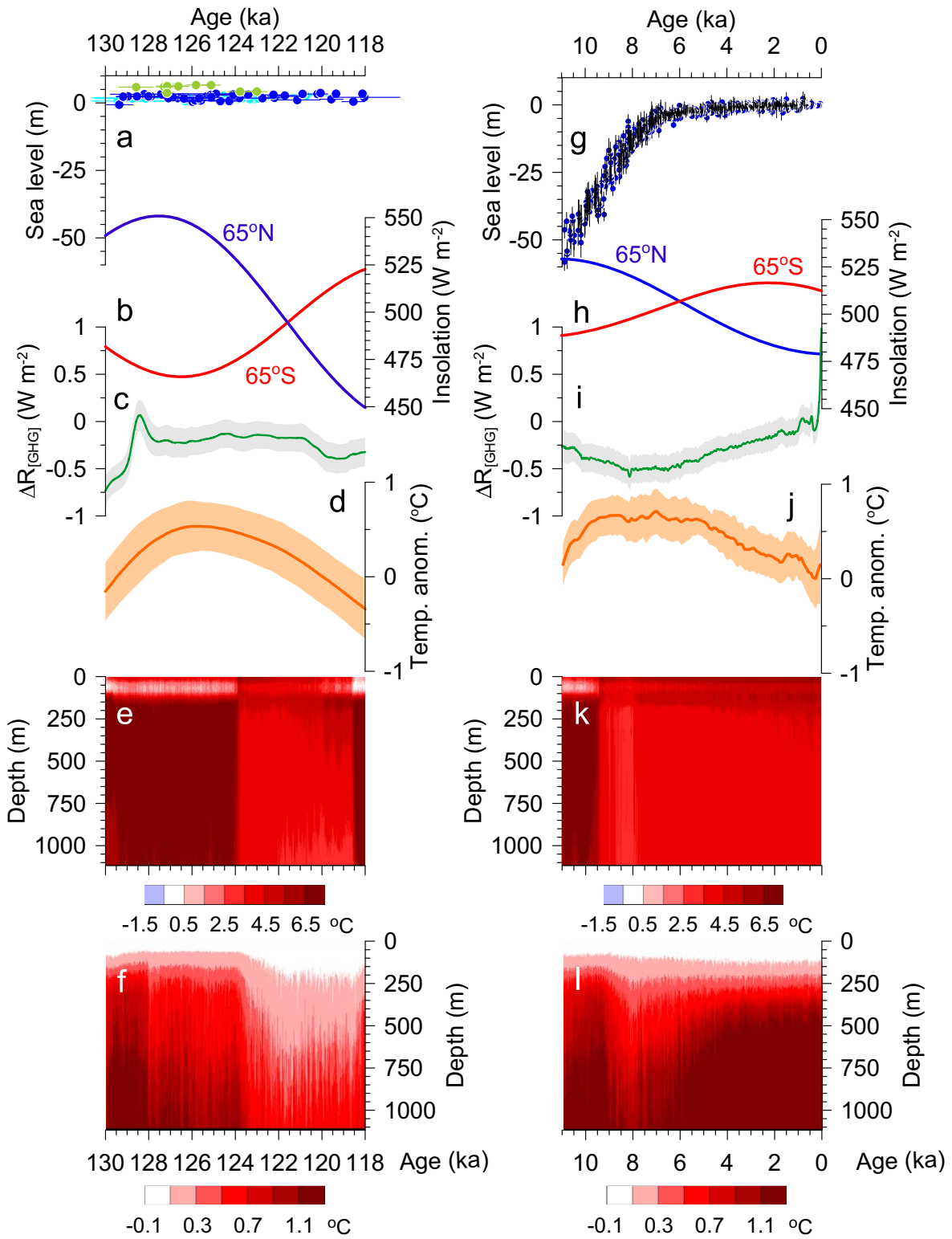
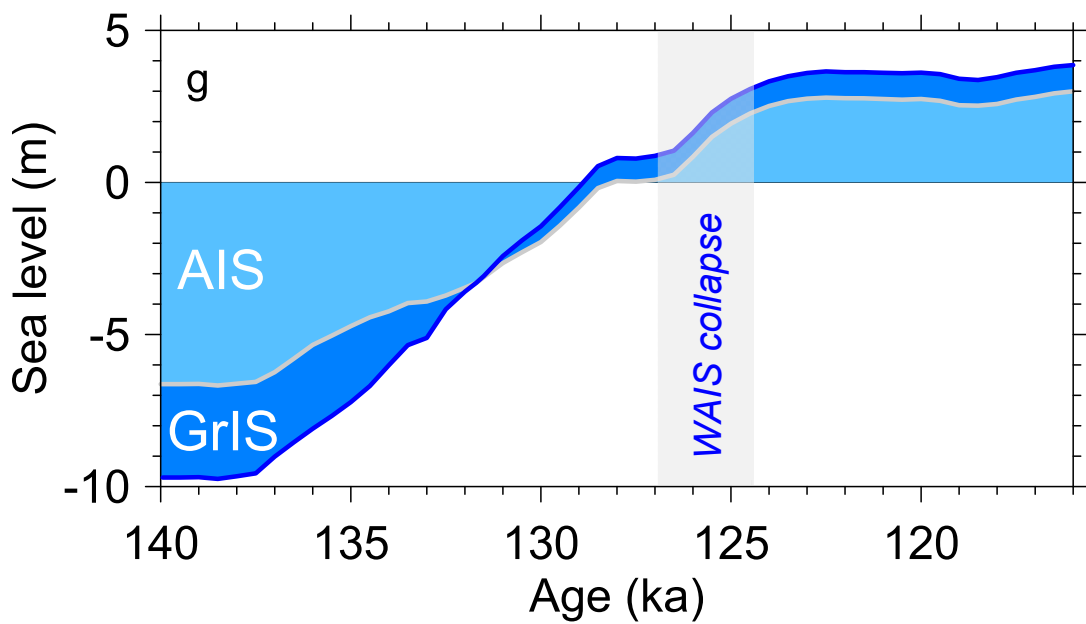
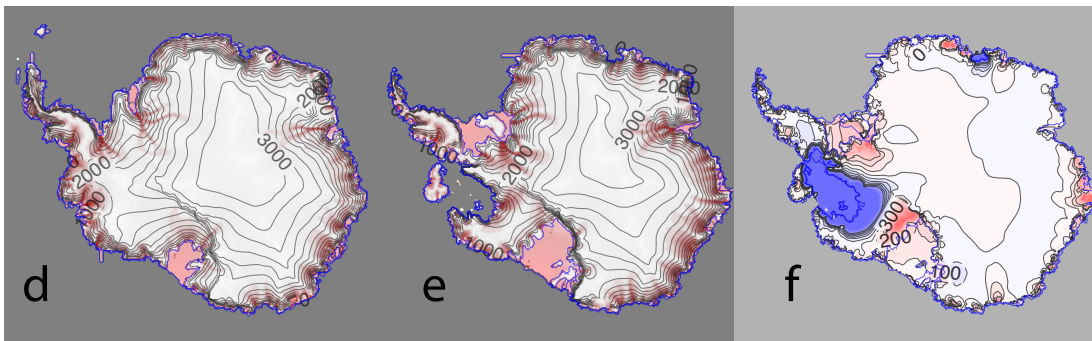
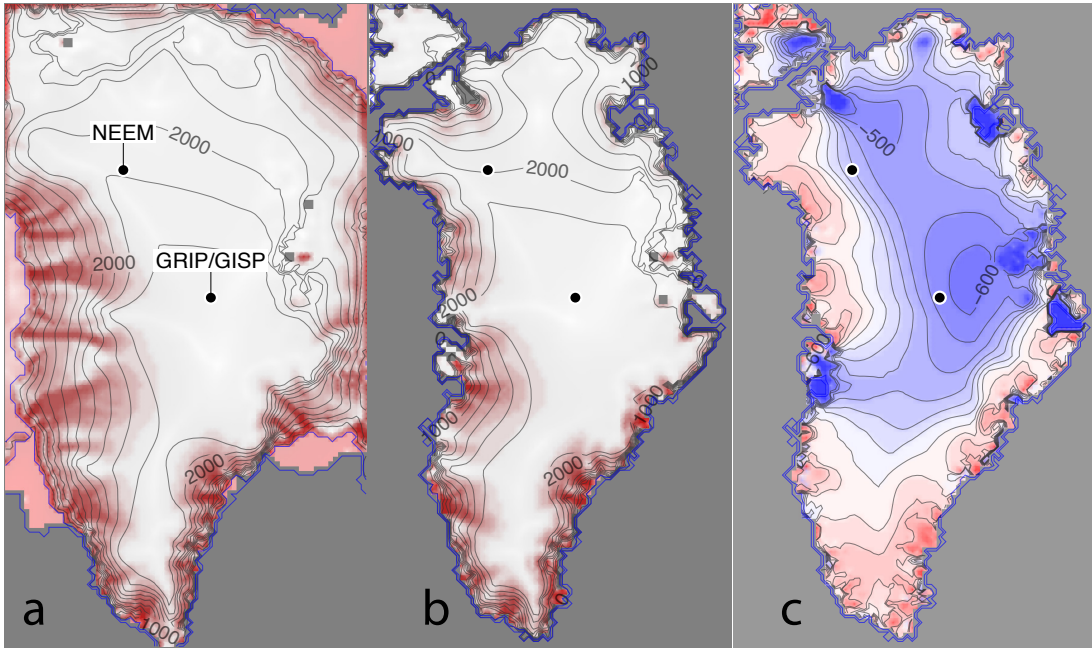
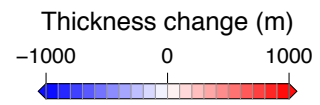
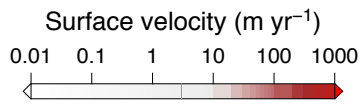


Figure 2



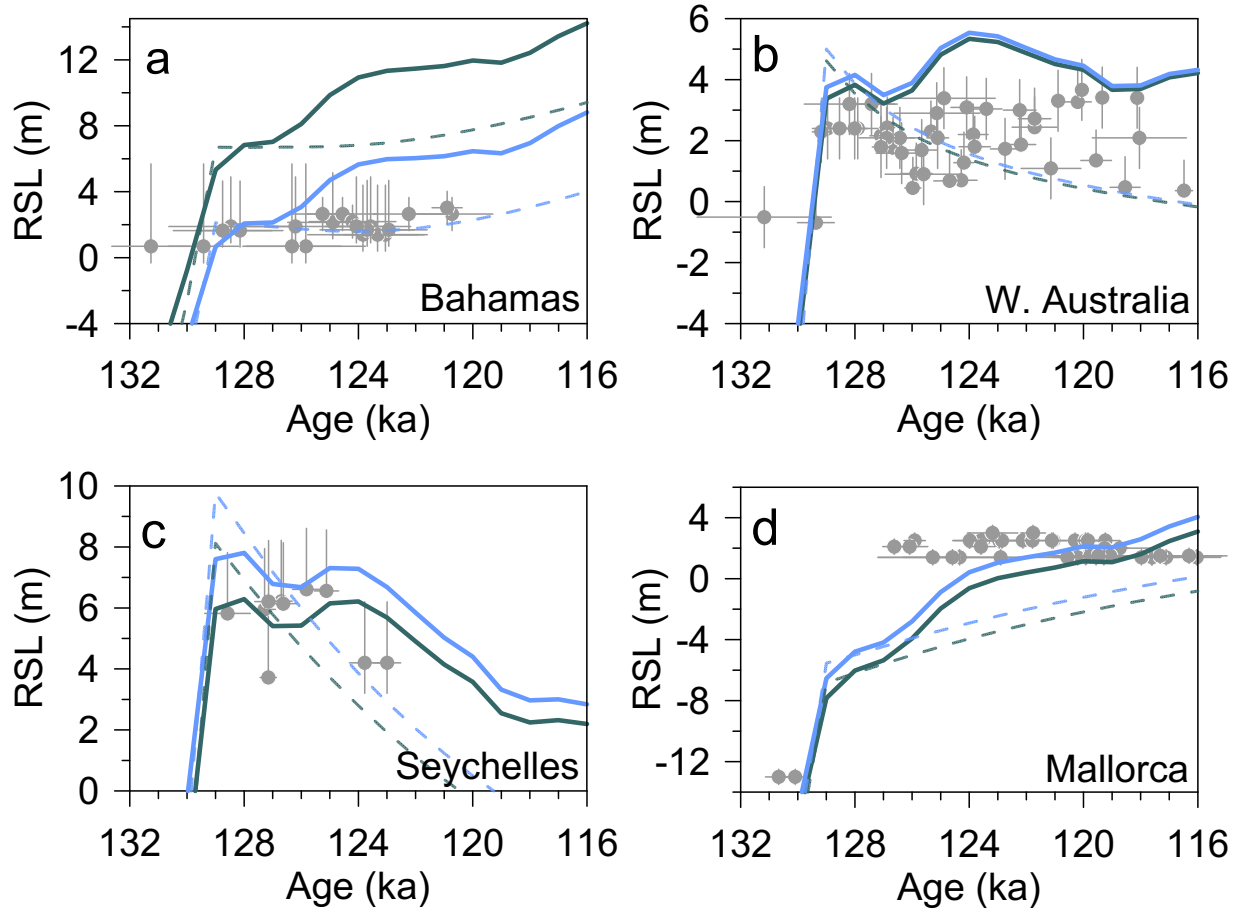
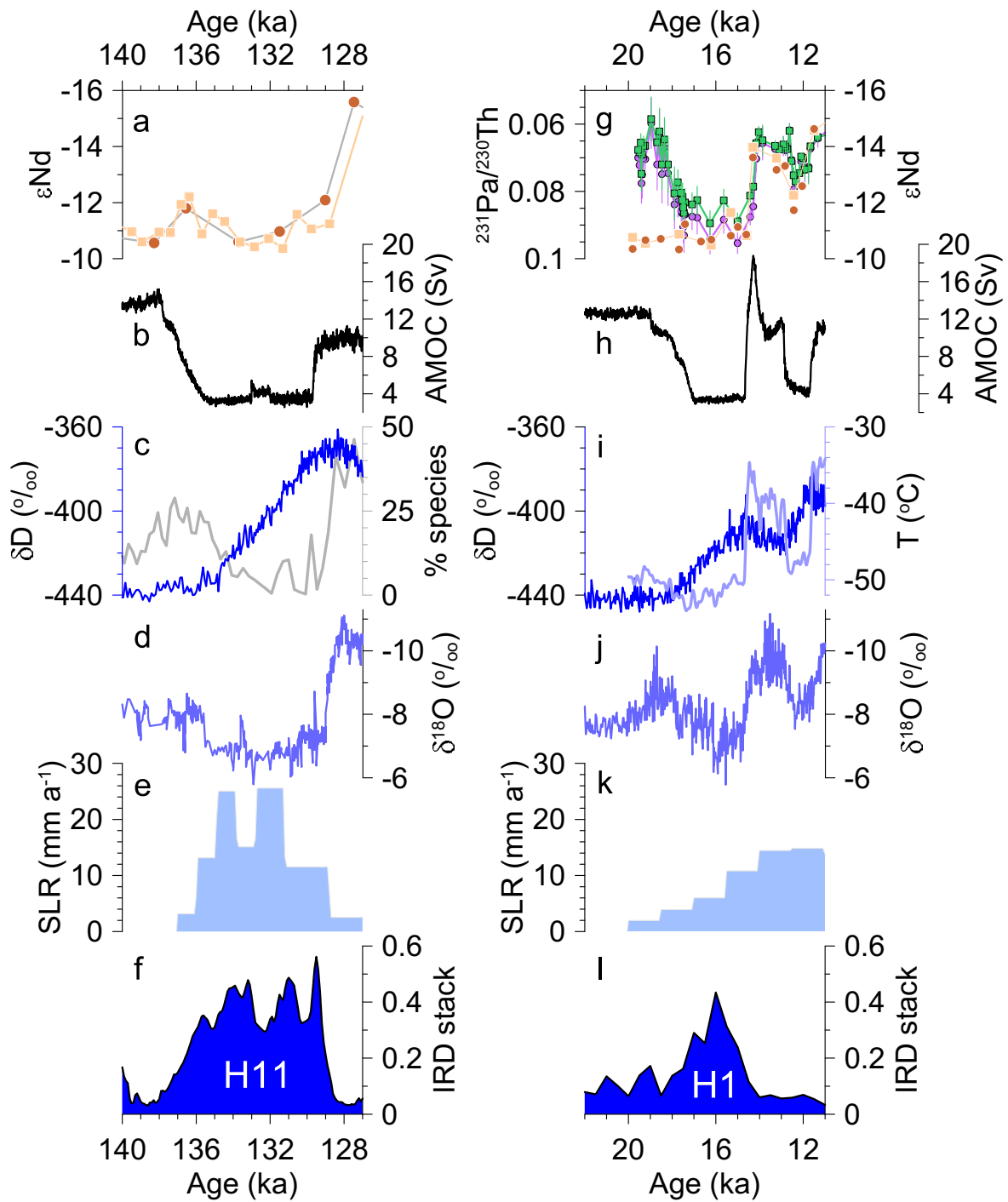
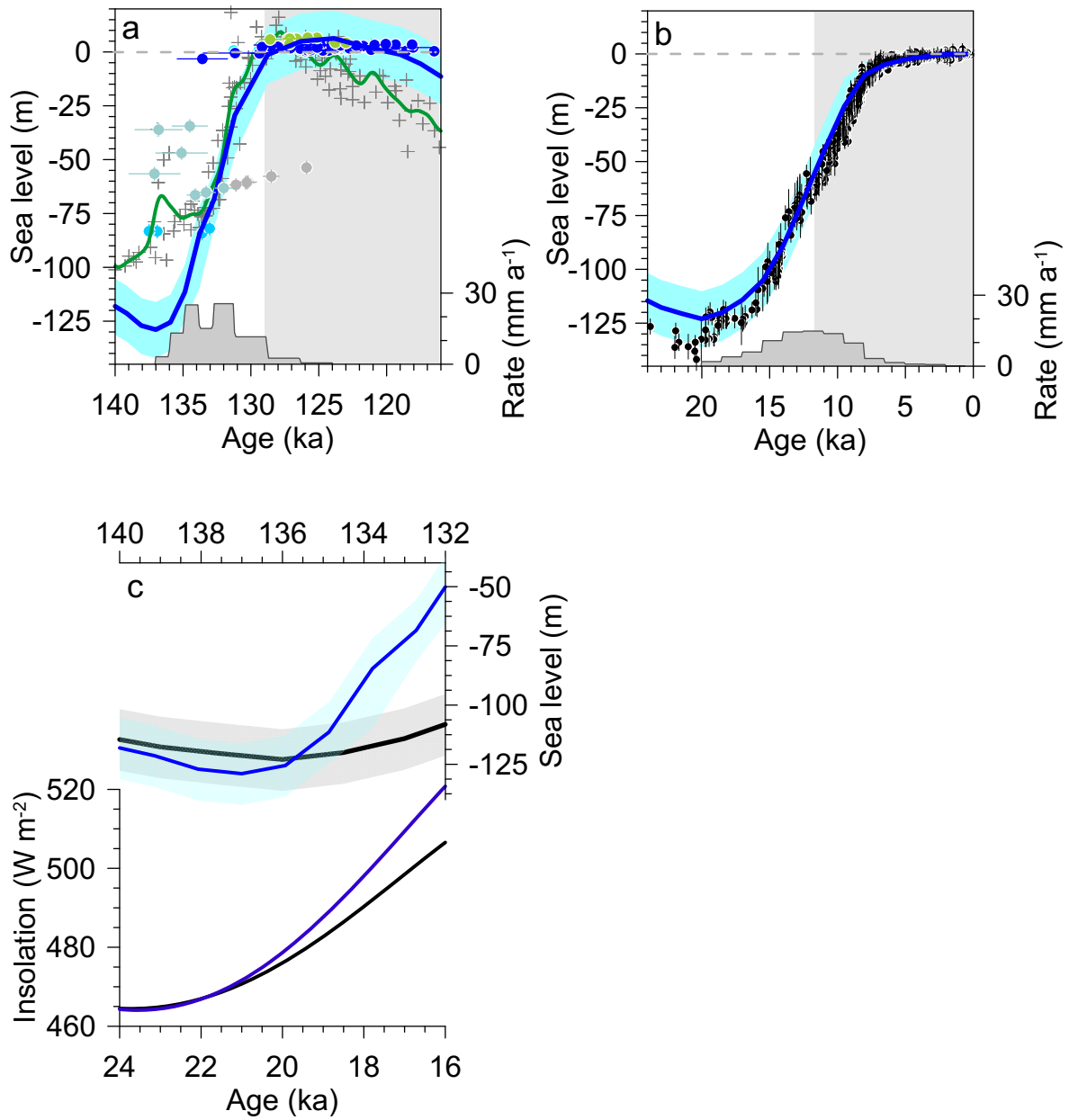


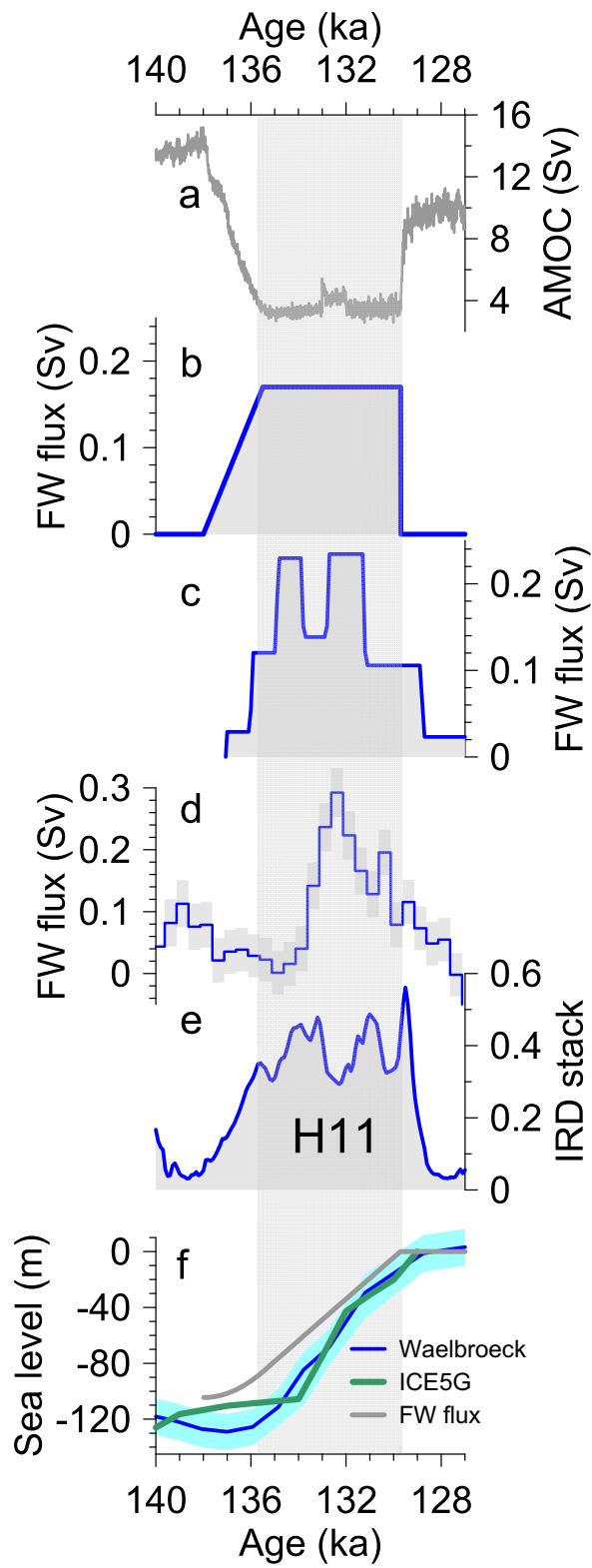
Figure 4



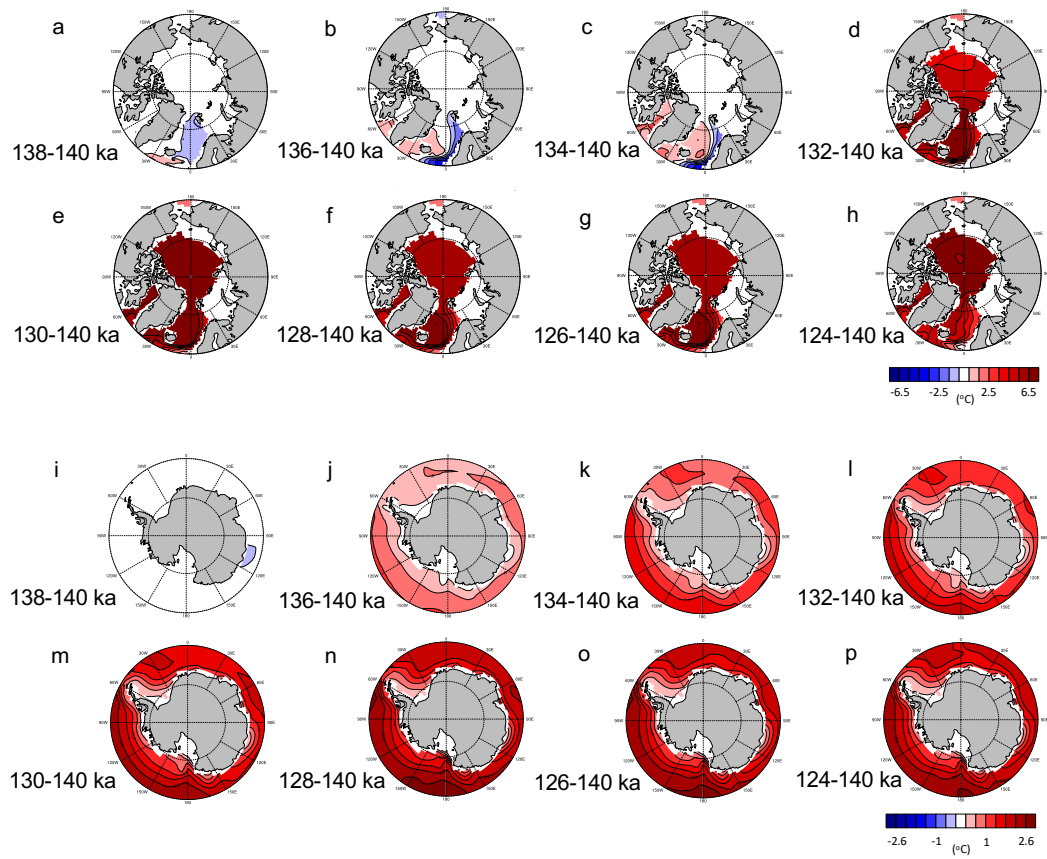
ED Fig. 1



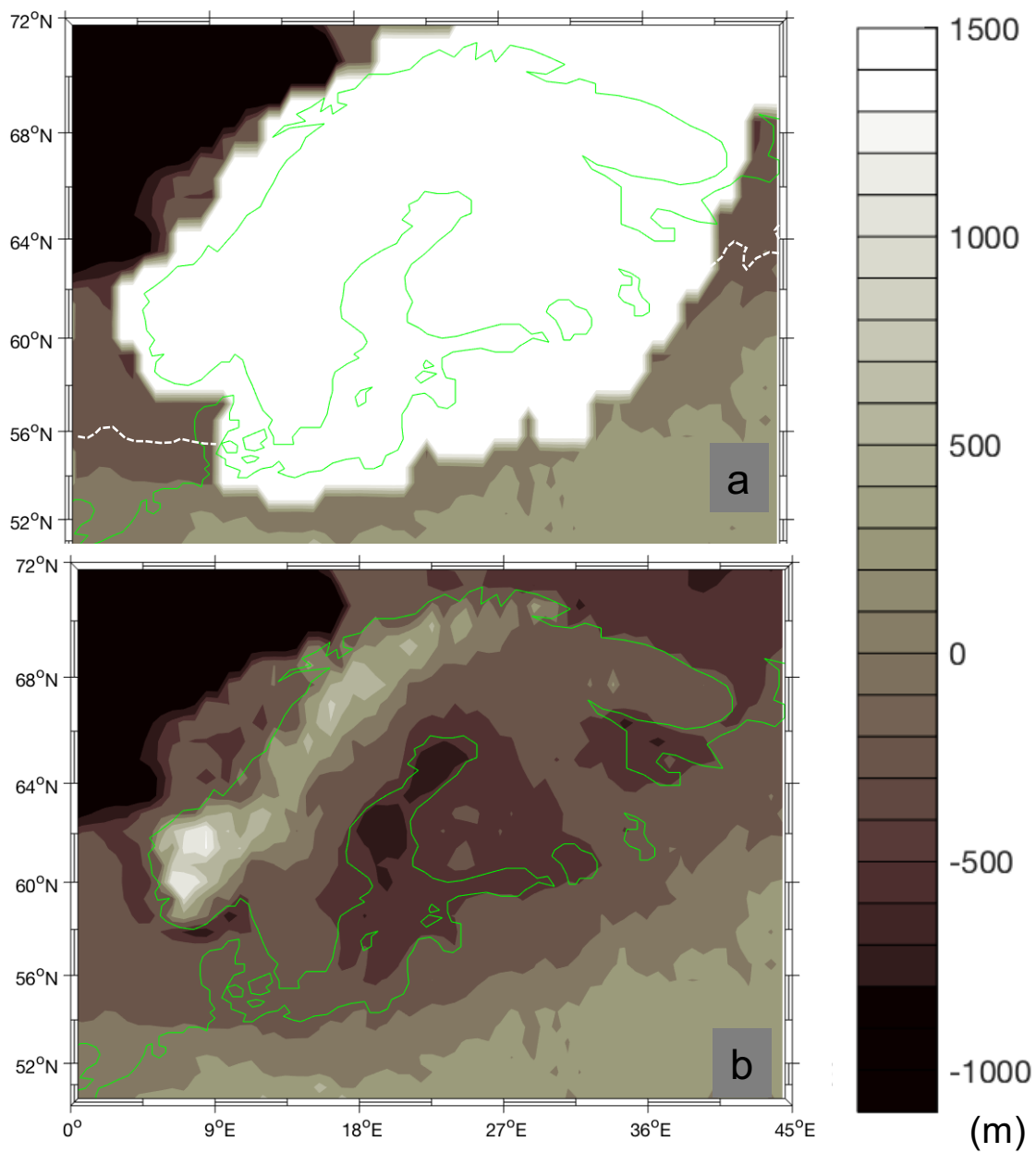
ED Fig. 2



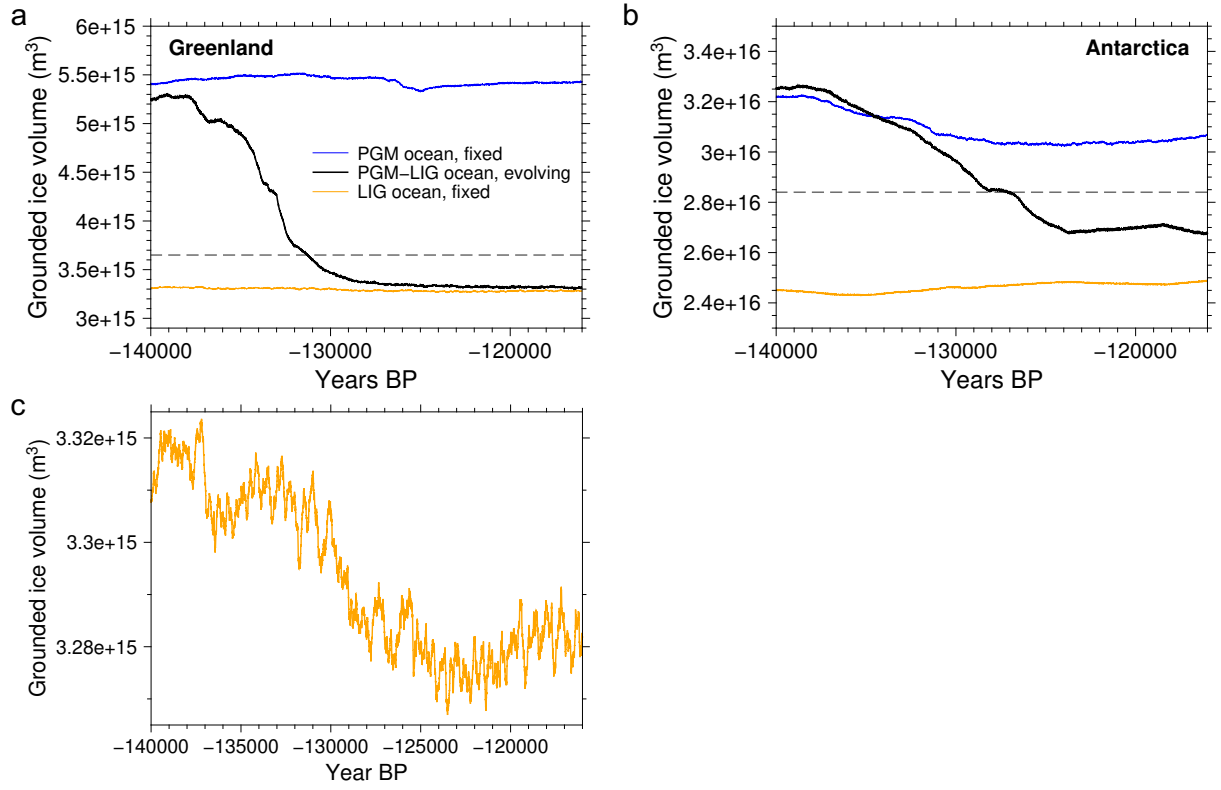
ED Fig. 3



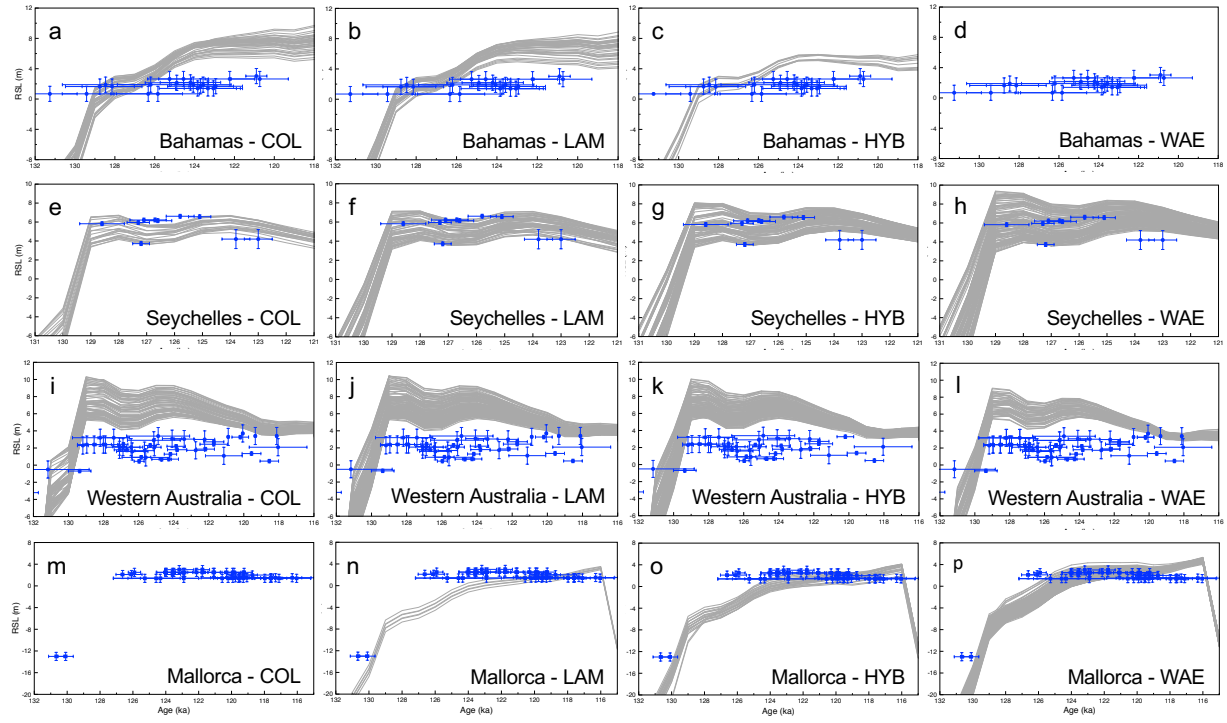
ED Fig. 4



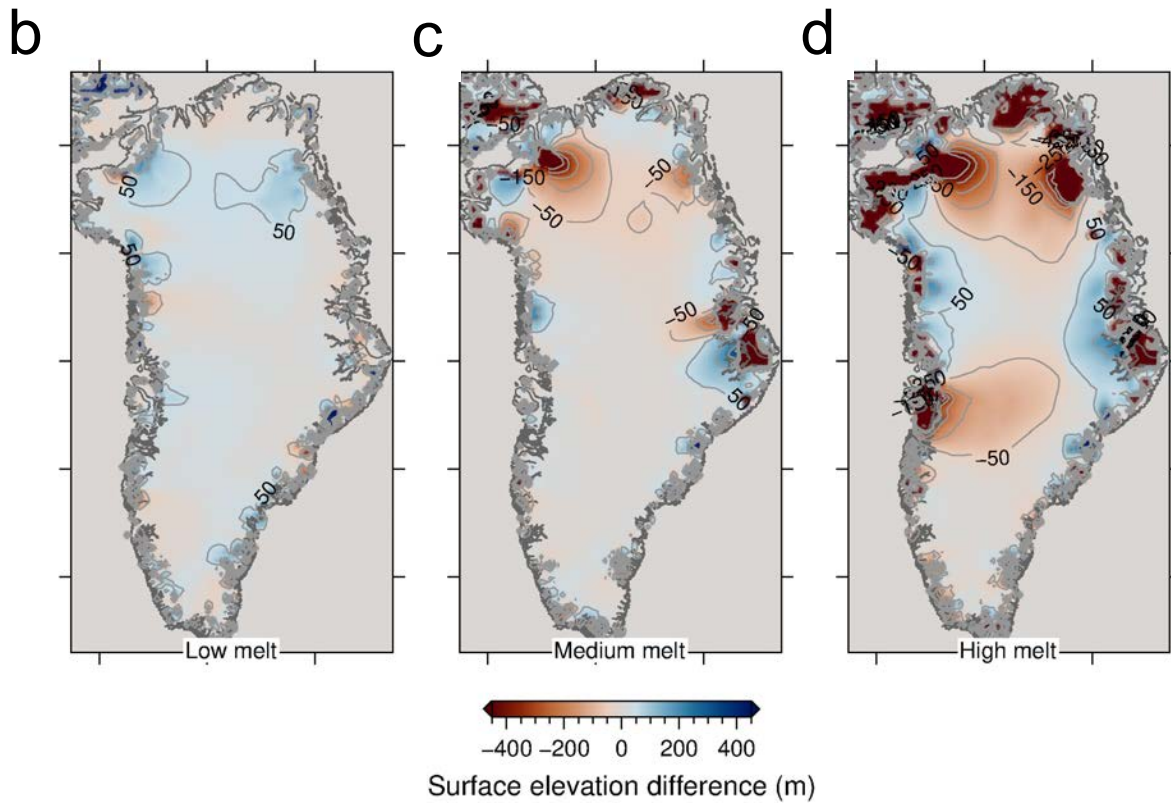
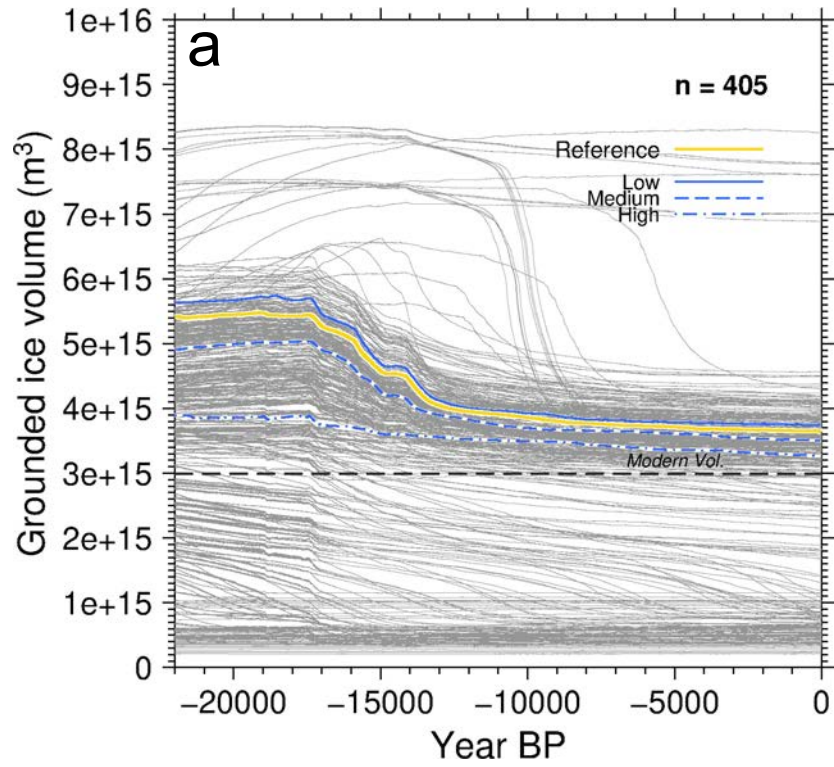
ED Fig. 5



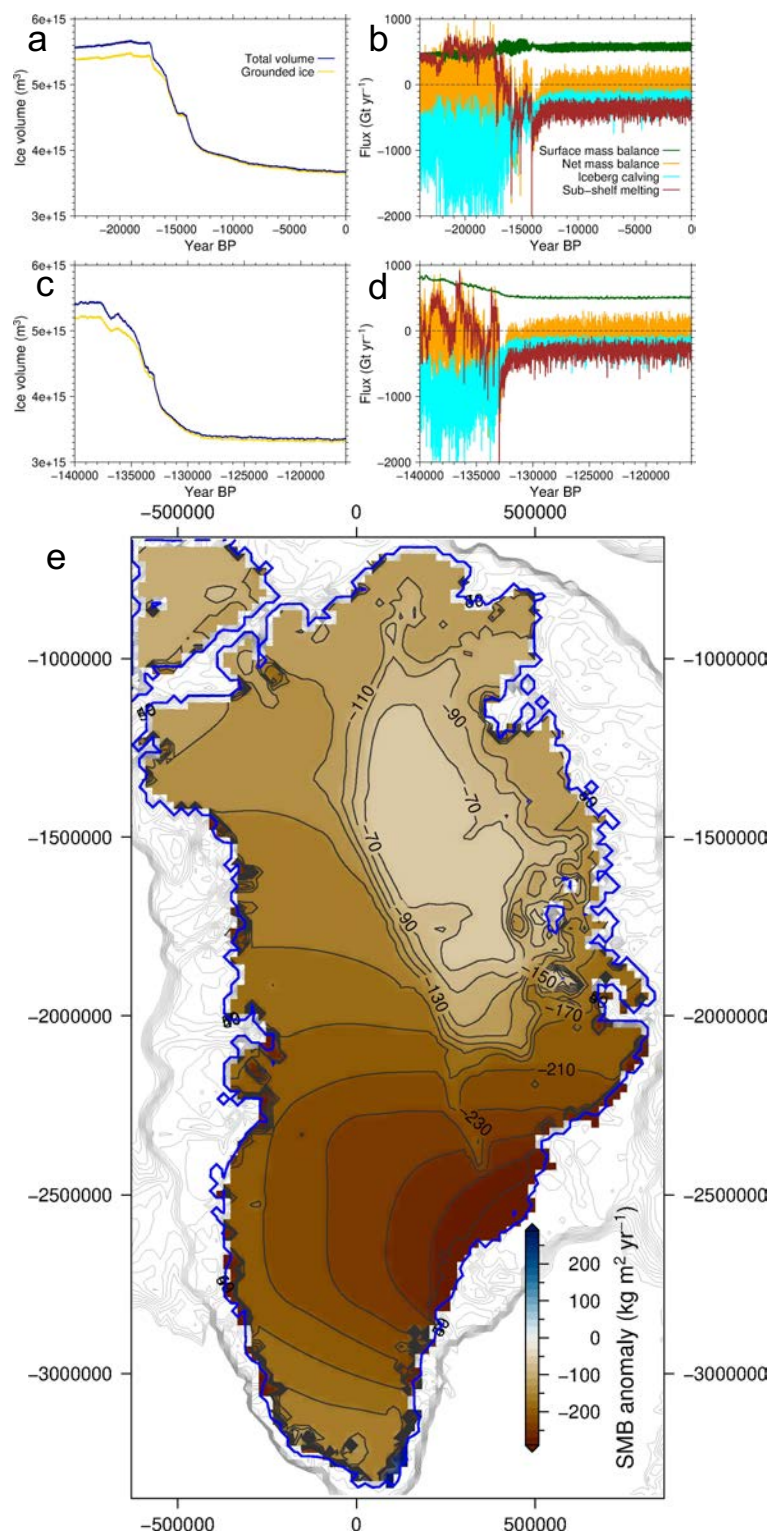
ED Fig. 6



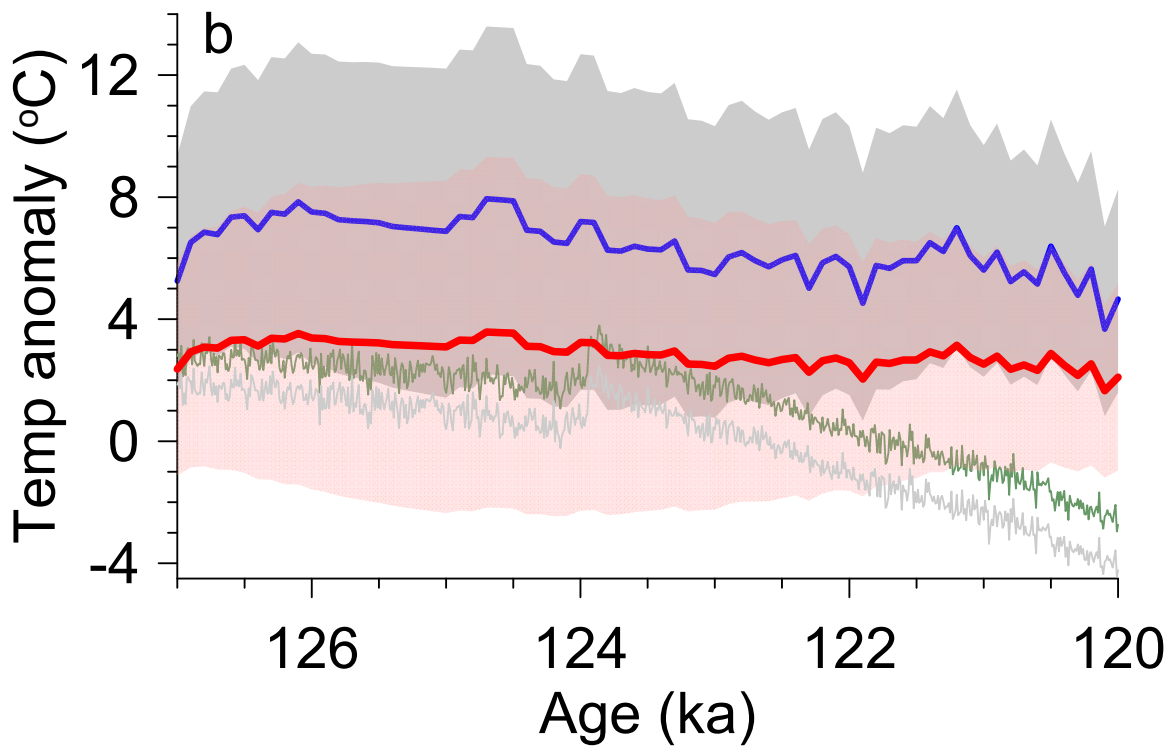
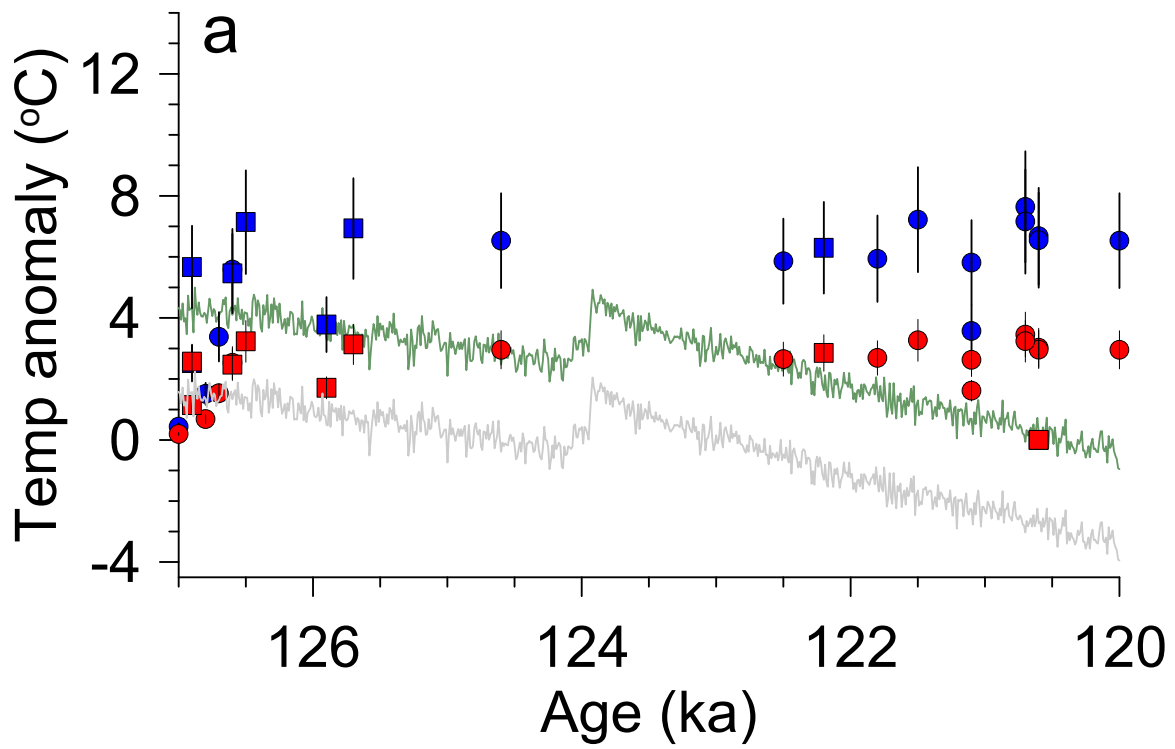
ED Fig. 7



ED Fig. 8



ED Fig. 9



ED Fig. 10